Non-Invasive Positron Detector to Monitor the Arterial Input Function in PET

VINCENT TURGEON

MEDICAL PHYSICS UNIT

MCGILL UNIVERSITY, MONTREAL

AUGUST, 2018

A thesis submitted to McGill University

in partial fulfillment of the requirements

for the degree of Master of Science

"You miss 100% of the shots you don't take - Wayne Gretsky."

-Michael Scott

ABSTRACT

Positron emission tomography (PET) is a nuclear medicine imaging modality used to acquire functional images. When several images are acquired at different time frames, the scan is considered dynamic, and the result is a movie showing where and how the imaging agents accumulated inside the patient. Dynamic PET is a valuable tool for staging and diagnosing of cancer, cerebral injuries and neurological disorders. To perform quantitative analysis on dynamic images, the imaging agent concentration in the arteries, known as the arterial input function (AIF), is required. The clinical standard to acquire the AIF is through invasive blood sampling. Unfortunately, the invasive withdrawal of arterial blood causes a significant discomfort to the patient and there is a risk of exposing the medical personnel to large amount of radiation. Since none of the alternative technologies and methods developed in the past 30 years were able to replace the manual blood sampling, dynamic PET imaging is restricted to centers with large financial and technical resources. We have developed a non-invasive and cost effective radiation detector based on plastic scintillating fibers to detect the positrons emerging from the patient's wrist arteries after the injection of the radiotracers and monitor the AIF. The first aim of this thesis was to characterize the attenuation length of the detector with ^{137}Cs and ultraviolet (UV) sources. The attenuation length obtained with ^{137}Cs agrees with the one provided by the scintillating fiber's manufacturer, but the measurement with UV source over-estimates it. The second aim was to investigate if the bending of the fiber in loops would cause important light losses. With the ^{137}Cs source, the losses were smaller than the measurement uncertainty. The final aim was to test the detector with ^{18}F and ^{11}C. The detector response to a pulse of radioactivity is better for the ^{11}C, due to its longer positron range. The detector was also able to accurately measure the decay of ^{11}C from 3.02 MBq/ml to 0.17 MBq/ml. These preliminary measurements demonstrate that plastic scintillating fibers are a suitable detection material to develop a non-invasive detector that could potentially replace invasive blood sampling as the clinical method to determine the AIF in dynamic PET imaging.

RÉSUMÉ

La tomographie par émission de positrons (TEP), est une modalité d'imagerie en médecine nucléaire utilisée pour obtenir des images fonctionnelles. Lorsque plusieurs images sont acquises à différents moments lors d'un scan, il s'agit d'un scan dynamique et le résultat est un film qui montre où et comment les agents d'imageries se sont accumulés dans le patient. La TEP dynamique est un outil indispensable dans le diagnostic du cancer, des traumatismes cérébraux et des maladies neurologiques. Afin d'obtenir des informations quantitatives à partir des images dynamiques, il est nécessaire de connaitre la concentration de radiotraceurs dans les artères, aussi connue comme la fonction d'entrée artérielle (FEA). Actuellement, la méthode standard pour obtenir la FEA est de prendre des échantillons de sang à différent moments lors du scan. Malheureusement, cette procédure invasive occasionne un important inconfort pour le patient en plus d'exposer le personnel médical prenant les échantillons à de la radiation ionisante. Puisqu'aucune solution proposée dans les 30 dernières années n'a pu s'établir comme nouveau standard clinique, la TEP dynamique est restreinte aux centres de recherche avec d'importantes ressources financières et techniques. Nous avons développé un détecteur non-invasif et à faibles coûts utilisant les fibres optiques scintillantes pour détecter directement les positrons provenant des artères du poignet afin d'obtenir la FEA. Premièrement, la longueur d'atténuation du détecteur a été mesurée avec une source de ^{137}Cs et une source ultraviolette (UV). La longueur d'atténuation obtenue avec la source de ^{137}Cs coïncide avec la valeur du fabricant, cependant, avec la source UV, la valeur est surestimée. Deuxièmement, les pertes de signal causées par l'enroulement de la fibre scintillante ont été étudié. Avec la source de ^{137}Cs, les pertes étaient plus petites que l'incertitude sur les mesures. Finalement, le détecteur a été testé avec du ^{18}F et du ^{11}C, deux radio-isotopes utilisés en TEP. Le signal pour un pulse de solution traversant le détecteur est beaucoup plus net avec le ^{11}C qu'avec le ^{18}F, notamment en raison de la plus grande portée de ses positrons. Aussi, le détecteur a été en mesure de mesurer exactement la constante de désintégration du ^{11}C pour une

activité variant de 3.02 MBq/ml à 0.17 MBq/ml. Suite au succès de ces tests initiaux, le détecteur sera testé sur des patients dans la prochaine année.

Acknowledgements

My first thank you goes to my mentor and supervisor Dr. Shirin Abbasinejad Enger. This project could not have been possible without her guidance and support. Her commitment to our research is one of the main reasons behind the success of this project. I would like to acknowledge the co-inventor of the detector, Dr. Gustavo Kertzscher. His previous work was the corner stone for the development of this detector. I would like to thank Dr. Gassan Massarweh, Robert Hopewell and their team at the Montreal Neurological Institute and Hospital, who provided lab space and the radioactive solutions. They handle the radioactivity as I do not have the proper training. Thanks to Michael Evans for his help with the radiation check source I needed during my experiments and to Joe Larkin and Bhavan Siva, who were always ready to repair my equipment. A special thank you goes out to my family, for their unconditional support during my entire academic progress. Finally, thank you to all my colleagues who gave their opinion and helped me solve countless issues. I also acknowledge partial support by the CREATE Medical Physics Research Training Network grant of the Natural Sciences and Engineering Research Council (Grant number: 432290) and from the Fond de Recherche Québec, Nature et Technologies (Grant number: 199601).

Contribution of Authors

Every chapter of this thesis was written by Vincent Turgeon. The main part of the thesis comes from experimental procedures performed at the McGill University Health Center and the Montreal Neurological Institute and Hospital.

For the experiments described in chapter 5, Dr. Gustavo Kertzscher created the protocol to build a scintillating fiber-based detector and gave general guidelines on the different measurements. Dr. Gassan Massarweh provided lab space, radionuclide and radio-chemists to manipulate the radioactive solutions. Dr. Shirin Abbasinejad Enger supervised the work and provided general guidance.

Contents

List of Figures

List of Tables

List of Abbreviations

A.U.	Arbitrary Unit
AIF	Arterial Input Function
BGO	Bismuth Germanium Oxide
FDG	FluDeoxyGlucose
FWHM	Full Width at Half Maximum
LOR	Line Of Response
LSO	Lutetium Oxyorthosilicate
MRI	Magnetic Resonance Imaging
PET	Positron Emission Tomography
PMMA	Poly(Methyl MethAcrylate)
PMT	PhotoMultiplier Tube
ROI	Region Of Interest
SiPM	Silicon PhotoMultiplier
SNR	Signal-to-Noise Ratio
SUV	Standardized Uptake Value
TAC	Time-Activity Curve
UV	Ultraviolet

Physical Constants

Avogadro's constant	$N_A = 6.022 \times 10^{23}\,\mathrm{mol}^{-1}$
elementary charge	$e = 1.602 \times 10^{-19}\,\mathrm{C}$
electron rest mass	$m_e = 9.11 \times 10^{-31}\,\mathrm{kg}$
Planck's constant	$h = 6.626 \times 10^{-34}\,\mathrm{J\,s}$
pi	$\pi = 3.141\,592\,6$
Speed of light in vacuum	$c = 2.998 \times 10^{8}\,\mathrm{m\,s}^{-1}$

List of Symbols

A	atomic mass number	
A	activity	Bq
C_i	radioactivity concentration in compartment i	$\mathrm{Bq\,mL^{-1}}$
C_{PET}	radioactivity concentration in PET pixel	$\mathrm{Bq\,mL^{-1}}$
E	energy	eV
E_B	binding energy	eV
E_K	kinetic energy	eV
E_{max}	maximum positron energy	eV
E_{mean}	average positron energy	eV
L	losses in light signal when bending fiber optic cables	%
$\mathcal{M}(Z, A)$	atomic mass	kg
N	neutrons	
P^+	protons	
Q_{β^+}	energy released in $beta^+$ decay	eV
R_0	PMT ratio when the scintillating fiber is straight	
R	PMT ratio when the scintillating fiber has a loop	
R_{max}	maximum positron range	mm
R_{mean}	average positron range	mm
S_0	normalization constant of the PMT signal	A.U.
$S(x)$	PMT signal at position x	A.U.
S_i	singlet state of electron	
T_i	triplet state of electron	
Z	atomic number	
$h\nu$	initial photon energy	eV
$h\nu'$	scattered photon energy	eV
k_{ij}	rate transfer constant between compartment i and j	min
n	index of refraction	
$t_{1/2}$	half-life	s
w	weight	kg
x	position of excitation source	cm
β	either positron or electron	
β^-	electron	
β^+	positron	
ε	relative photon energy	
θ	photon scattering angle	rad
θ_C	critical angle for total internal reflection	rad
θ_R	angular distribution in Rayleigh scattering	rad
λ	decay constant	$\mathrm{s^{-1}}$
λ_a	1/e attenuation length	cm

μ_γ	photon absorption coefficient	cm^{-1}
ν	neutrino	
ϕ	electron recoil angle	rad

Dedicated to: Estelle for how much she inspires me to be better, Douglas for being the most curious mind I know and Julius, for all the support he brought me since I met him.

Chapter 1

Ionizing Radiation

The Oxford English Dictionary defines radiation as "the emission of energy as electromagnetic waves or as moving subatomic particles" (Online, 2010). When the radiation has enough energy to strip an electron from the atoms it interacts with, it is called ionizing radiation. Observed for the first time in 1895 by Wilhelm Röntgen (Rontgen and W. C., 1896), ionizing radiation has been studied for over a century and plays now a major role in medicine and high energy physics. This chapter will cover the interactions with matter of two types of ionizing radiation: photons and light charged particles.

1.1 Photon interactions

1.1.1 Thomson scattering

The scattering of a photon by "loosely" bound electron is adequately described by the non-relativistic theory developed by Joseph J. Thomson. A "tightly" or "loosely" bound electron refers to the difference between the electron's binding energy and the incident photon's energy. If the photon's energy is much higher than the binding energy, the electron is loosely bound. If the energies are on the same order, the electron is tightly bound. In Thomson scattering, the photon changes direction without losing energy,

but this interaction is only valid for photons with an energy $h\nu$ much smaller than the rest mass of the electron (i.e. 511 keV) (Podgorsak, 2006).

1.1.2 Compton scattering

Compton scattering is defined as a process where a photon with energy $h\nu$ interacts with a stationary and loosely bound orbital electron and transfers part of its energy to the electron. The result is a photon with energy $h\nu'$ scattered at angle θ and a recoil electron with kinetic energy E_K scattered at angle ϕ, as shown in figure 1.1.

One can calculate the energy of the scattered photon and the recoil electron as well as the angles θ and ϕ using the conservation of energy and momentum. The results are:

$$h\nu' = h\nu \cdot \frac{1}{1+\varepsilon(1-\cos\theta)} \tag{1.1}$$

$$E_K = h\nu \cdot \frac{\varepsilon(1-\cos\theta)}{1+\varepsilon(1-\cos\theta)} \tag{1.2}$$

Where, ε is the initial photon energy normalized by the electron mass energy $m_e c^2 =$ 511 keV. The relationship between the photon and recoil electron scattering angles is displayed in equation 1.3 (Podgorsak, 2006).

$$\tan\phi = \frac{1}{1+\varepsilon}\cot\frac{\theta}{2} \tag{1.3}$$

1.1.3 Rayleigh scattering

The theory for the scattering of electromagnetic radiation on strongly bound atomic electrons was developed in 1900 by John W. Rayleigh. The energy transferred in this interaction is negligible. The scattered photon has essentially the same energy, and the atom is neither ionized nor excited. The angular distribution of Rayleigh scattering,

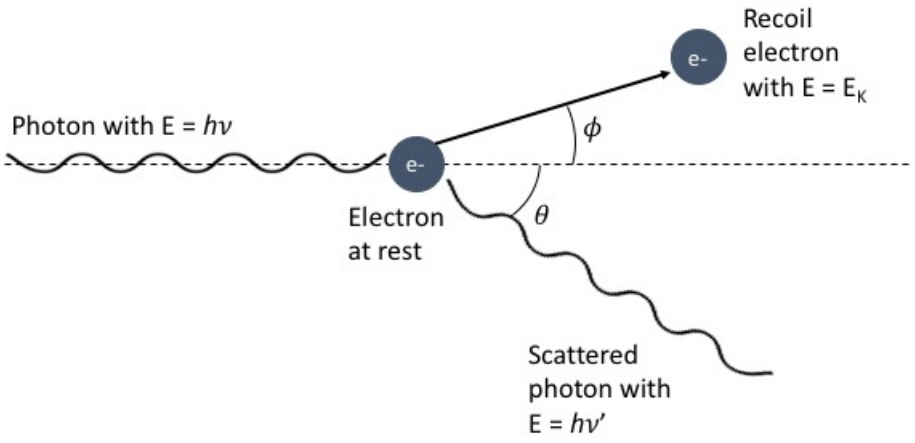

FIGURE 1.1: Representation of Compton scattering. A photon incident on a stationary electron will result in a scattered photon of lower energy and a recoil electron.

meaning the half-angle of a cone containing 75% of the scattered photons is estimated by equation 1.4:

$$\theta_R \approx 2\text{arcsin}(\frac{0.026Z^{\frac{1}{3}}}{\varepsilon}) \tag{1.4}$$

Where Z is the atomic number of the absorber and ε is the photon energy normalized to the electron rest mass energy. The effective Z for soft tissue is approximately 7 (Kurudirek, 2014), resulting in $\theta \approx 5.7°$. Rayleigh scattering is not as important as the other photon interactions (Podgorsak, 2006).

1.1.4 Photo-electric effect

This interaction occurs between a photon and a tightly bound orbital electron. The photon is completely absorbed and its energy transferred to the electron. The electron kinetic energy is given by:

$$E_K = h\nu - E_B \tag{1.5}$$

Where E_B is the electron binding energy. A schematic representation of a photon interacting with a K-shell electron is depicted in figure 1.2. The vacancy created in the orbital shell will be filled by an electron of a higher shell, resulting in the emission of characteristic fluorescence or an Auger electron (Podgorsak, 2006).

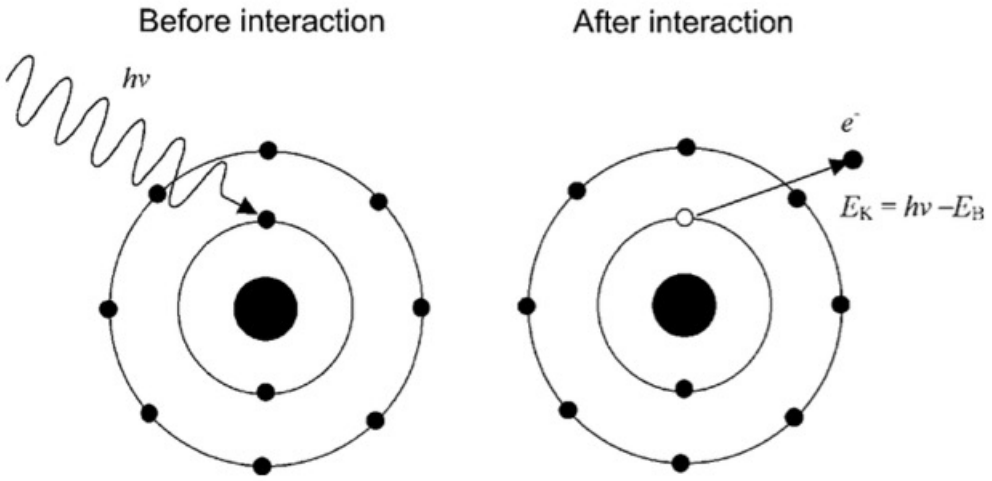

FIGURE 1.2: Representation of the photo-electric effect. The photon energy hν exceeds the binding energy E_B and the electron is ejected with a kinetic energy E_K. Figure from Podgorsak, 2006.

1.1.5 Pair and triplet production

Pair production occurs when a photon with energy $h\nu$ larger than $2m_ec^2$ interacts with the field of the nucleus to disappear and create an electron-positron pair. Triplet production also results in the creation of an electron-positron pair, but this interaction is with the field of an orbital electron. The minimum threshold for triplet production is $4m_ec^2$, and the orbital electron is also ejected, similar to the photo-electric effect (Podgorsak, 2006).

1.1.6 Photo-nuclear reactions

Photo-nuclear reactions are also called nuclear photo-electric effect or photo-disintegration. When a nucleus absorbs a photon, it can emit different radiation: a single neutron, protons, alpha particles, gamma rays or even more than one neutron. The threshold photon energy required for these reactions depends on the nucleus, but the smallest is 2.225 MeV for ^{2}H (Podgorsak, 2006).

1.1.7 Probability of interaction

The probability of each interaction depends on the material the photon is traversing and on the photon kinetic energy. Figure 1.3 illustrates the most probable interaction for different atomic numbers over the range of energy relevant to nuclear medicine. Due to the small effective atomic number of human soft tissue, the dominant interaction between photons and human tissue is the Compton scattering (Cherry, Sorenson, and Phelps, 2012).

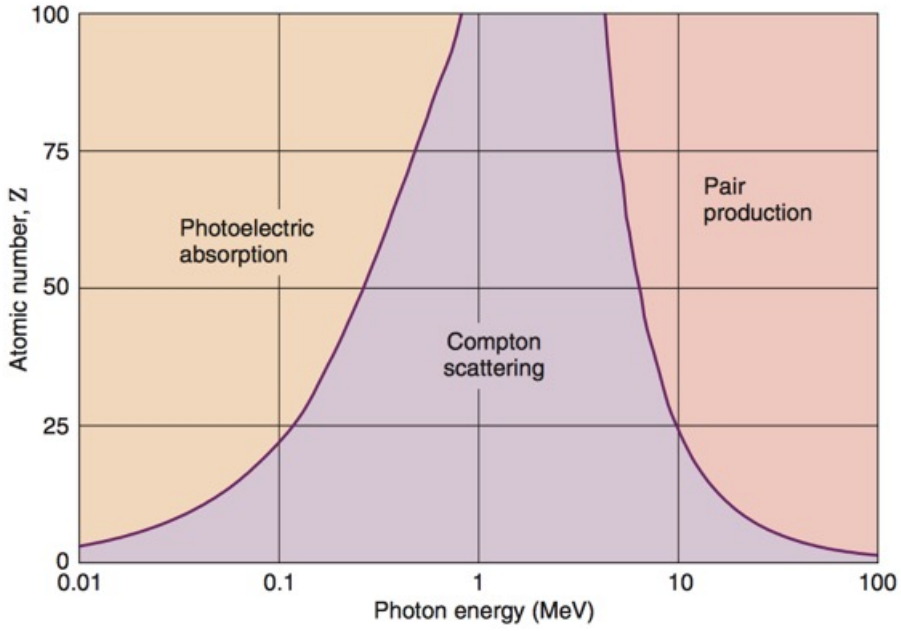

FIGURE 1.3: Most probable photon interaction as a function of photon energy and atomic number of the absorbing material. Figure obtained from Cherry, Sorenson, and Phelps, 2012.

1.2 Light charged particles

A charged particle moving through a medium undergoes Coulomb interactions with the atoms in the medium. The smallest distance between the charged particle and the nucleus of the atom it is interacting with, is known as the *classical impact parameter* b, and dictates the type of collision, as shown in figure 1.4. First, if b is on the same order as the atom's radius, the incoming particle will transfer a significant amount of energy to a single orbital electron. The orbital electron will have enough energy to have Coulomb interactions with other atoms in the medium. This interactions is known as a hard collision. Second, if the impact parameter is much larger than the atom's radius, the collision is soft, meaning that the particle interacts with the whole atom. The energy transfer is small, but there is a large number of soft collision resulting in polarizations, excitations and ionizations of the medium's atoms. Finally, if the impact parameter is small compared to the atom's radius, a radiation collision occurs, where the particle interacts with the atom's nucleus. This interaction results in elastic or inelastic scattering. In elastic scattering, the particle changes direction, but only transfer a negligible amount of energy. However, in inelastic scattering, the amount of energy loss can be significant and result in the emission of x-rays. Radiation collisions are also known as radiative losses or as bremsstrahlung collisions and they are responsible for the production of diagnostic and therapeutic x-rays (Podgorsak, 2006).

1.2.1 Stopping power and range

As the light charged particle travels through a medium, it undergoes a large number of the previously mentioned interactions before losing its kinetic energy completely. The rate of energy loss per cm traveled in the medium divided by the medium's density ρ is called the mass stopping power S:

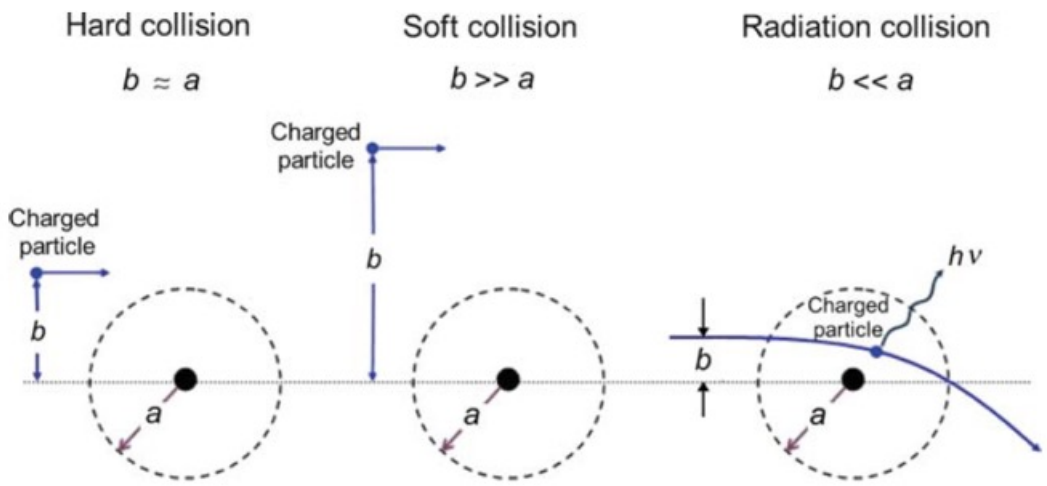

FIGURE 1.4: Different types of collisions for charged particles depending on the classical impact parameters b and the classical atom radius a. Figure from Podgorsak, 2006.

$$S = \frac{1}{\rho}\frac{-dE}{dx} \tag{1.6}$$

The total mass stopping power includes losses of energy from hard, soft and radiation collisions. The importance of collisions and radiative stopping power depends on the charged particle kinetic energy and the absorbing medium atomic number. The critical energy E_{crit} where both stopping powers are equal can be estimated with (Podgorsak, 2006):

$$E_{crit} \approx \frac{800\text{MeV}}{Z} \tag{1.7}$$

As expressed in equation 1.6, the distance traveled by a light charged particle in a medium can be obtained by integrating the mass stopping power over the kinetic energy of the particle:

$$\text{Range} \approx \int_0^{E_{init}} \frac{dE}{S(E)} \tag{1.8}$$

Meaning that particle's kinetic energy and the atomic number of the material will also affect the range the particle can travel in the material (Podgorsak, 2006).

1.3 Positron physics

1.3.1 Radioactive decay

An unstable nucleus transforms itself into a more stable one by converting mass into energy and emitting lighter particles, photons or even both. Alpha emission, nuclear fission, β^+ and β^- decay, internal conversion and electron capture are all different forms of radioactive decay and are described in details in (Cherry, Sorenson, and Phelps, 2012a). It is a spontaneous process that can only be described with probabilities. The average decay rate of a radioactive sample is given by:

$$\frac{\Delta N}{\Delta t} = -\lambda N = A \tag{1.9}$$

In equation 1.9, N is the number of radioactive atoms in the sample, t is the time and λ is the decay constant for this atom with units of s^{-1}. The average decay rate is the activity of the sample. The symbol for activity is A and the SI unit for activity is the Becquerel (Bq). Therefore the activity A can be obtained by integrating equation 1.9:

$$\int_0^t \frac{dN}{N} = \int_0^t -\lambda dt \rightarrow A(t) = A(0)e^{-\lambda t} \tag{1.10}$$

The time it takes a radioactive sample to decay to half its original activity is known as the half-life $t_{1/2}$ and is related to the decay constant by:

$$t_{1/2} = \frac{ln(2)}{\lambda} \tag{1.11}$$

1.3.2 Positron decay

The positron is the electron anti-particle. Both particles have the same mass, but equal and opposite charge, + and - $1.602 \cdot 10^{-19}$ C respectively. The radioactive emission of positrons is known as beta plus (β^+) decay. This decay happens in atoms that are proton-rich, meaning the atoms require the conversion of a proton into a neutron to become stable. Equation 1.12 describes the decay process. The energy released in the reaction is represented by the equation 1.13. The released energy Q_{β^+} is shared by the positron and the neutrino (ν), but this sharing of energy is not always the same. This is the reason why the positron energy from the beta plus decay is a spectrum rather than discrete as shown in the figure 1.5 (Podgorsak, 2006).

$$P^+ \rightarrow N + \beta^+ + \nu + Q_{\beta^+} \tag{1.12}$$

Where P^+ represents a proton, N represents a neutron, β^+ is the positron, ν is the neutrino and Q_{β^+} is the kinetic energy shared between the positron and the neutrino given as:

$$Q_{\beta^+} = \mathcal{M}(Z, A)c^2 - [\mathcal{M}(Z-1, A) + 2m_e]c^2 \tag{1.13}$$

With $\mathcal{M}(Z, A)$ being the atomic mass of the parent, $M(Z-1, A)$ the atomic mass of the daughter and $2m_e$ is twice the rest mass of the electron.

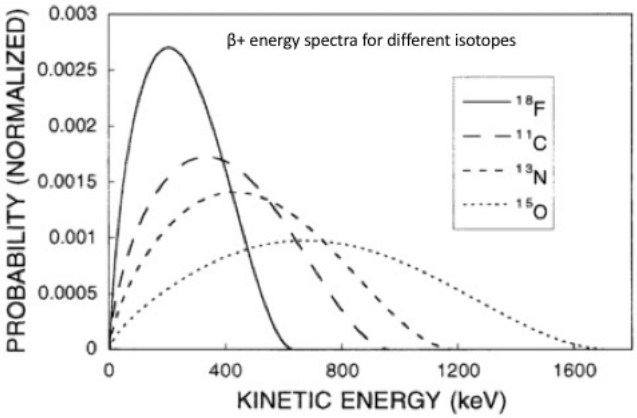

FIGURE 1.5: Theoretical energy of positron emitted by different radio-isotopes used in PET. Figure taken from Levin and Hoffman, 1999.

1.3.3 Positron annihilation

After the emission, the positron will lose its kinetic energy in radiative losses caused by Coulomb interactions with the nuclei and through collisions with the orbital electrons of the material it is going through. The term annihilation refers to the event where the electron and positron mass energy are converted into two photons of the same energy. Most electron-positron annihilations happen when the positron has lost all its kinetic energy and interacts with an orbital electron which is considered to be free and stationary. To ensure the conservation of charge, momentum and energy, two photons with the energy 511 keV are emitted in opposite directions at the site of the annihilation (Podgorsak, 2006). The free and stationary electron is an approximation, therefore the angle between both photons is not exactly 180°. The angular distribution around 180° has a full width at half maximum (FWHM) of 0.25° (Khalil, 2010b). The distance traveled by the positron in the material, from the emitting nuclei to the site of annihilation is called the range and depends on the positron kinetic energy and the material, as stated in section 1.2. The positron range and the non-collinearity both play a role in the spatial resolution of PET images. A schematic of the positron decay and annihilation is presented in figure 1.6.

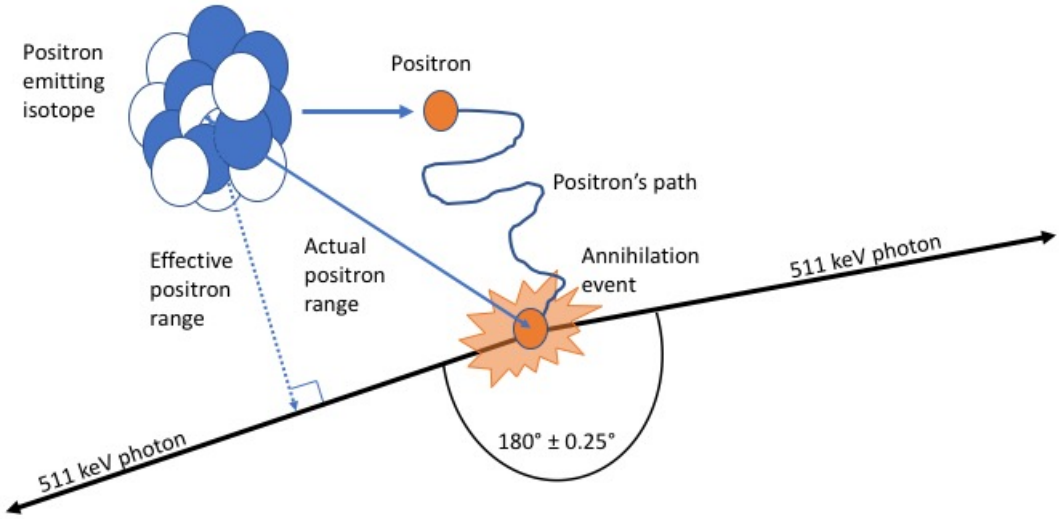

FIGURE 1.6: Schematic representation of the positron being emitted from the unstable nucleus, losing its kinetic energy and undergo annihilation. The two 511 keV photons are almost collinear, with the angular distribution having a FWHM of 0.25°. Figure adapted from Khalil, 2010b.

Chapter 2

Radiation Detectors

When radiation transverses a material, it transfers energy to the atoms of the material by ionization or excitation. Ionization occurs when an electron is stripped from the atom, resulting in a positively charged ion and a free electron. Excitation occurs when the energy transfer only changes the atom's electronic configuration, leaving the atom in an excited state. These two processes are involved in the detection of radiation. This chapter will present common radiation detectors used in medical physics and nuclear medicine, but is not an exhaustive list.

2.1 Gas-filled detectors

Gas-filled detectors measure the current that is generated between the electrodes of a capacitor. The opposite charges on each electrodes create an electric field between the electrodes. This system is in equilibrium and the medium between the plates, which can be air or a pressurized gas acts as an insulator. There is no charge circulating between the electrodes. When ionizing radiation passes between the electrodes, it ionizes the atoms. The positive ions are attracted to the negative electrode and the electrons are pulled towards the positive electrode, creating a measurable current. A representation of this principle is illustrated in figure 2.1. This current can be related to the

amount of radiation that passed through the detector (Cherry, Sorenson, and Phelps, 2012b).

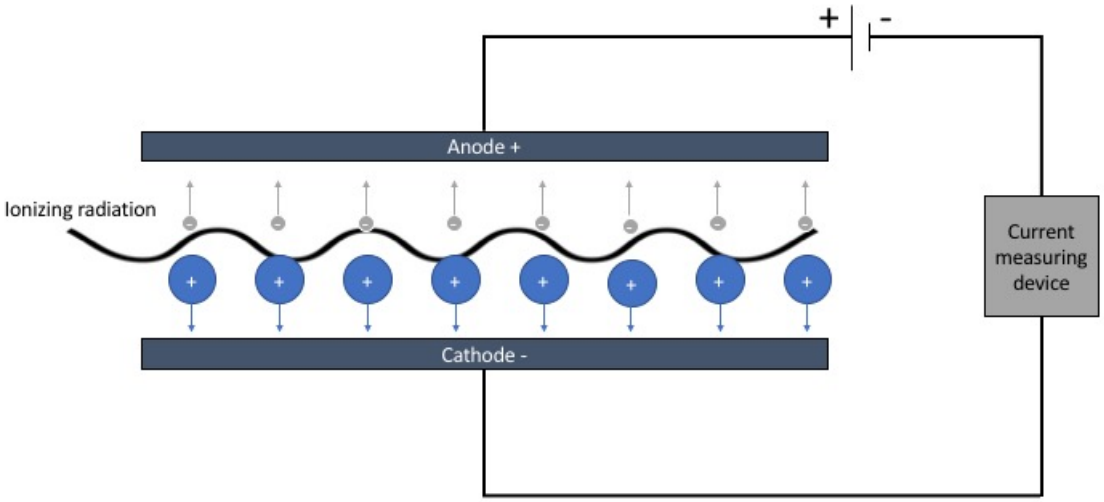

FIGURE 2.1: Schematic of the capacitor used for gas filled detector. The ionizing radiation passing between the electrodes creates positive ions and negative electrons that induced a current between the plates. The electrodes are presented as plates, but they can be in any geometry. Figure adapted from Cherry, Sorenson, and Phelps, 2012b.

2.1.1 Ionization chambers

If the voltage applied to the electrodes is on the order of 50 to 500 V (depending on the geometry), the gas filled detector is considered an ionization chamber. If the voltage is lower, recombination will occur. Recombination occurs when the ion and the electron recombine with each other, not contributing to the current. In dry air, one of the most common medium for ionization chambers, the mean energy needed to create an ion-electron pair is 33.97 eV (Attix, 2007). If a 1 MeV particle interacts within the air in the chamber before being stopped, it produces roughly $3{\cdot}10^{4}$ ionization, resulting in $3{\cdot}10^{-15}$ C. Since the amount of charge is very low, ionization chambers are not usually used for the detection of single radiation count, but rather to measure the total amount of charge collected by a radiation beam. This type of detector is mostly used for calibration of

radiation therapy beams and can be filled with ambient air or with a pressurized gas to increase the sensibility and eliminate the variability when the atmospheric pressure and temperature changes (Cherry, Sorenson, and Phelps, 2012b).

2.1.2 Proportional counters

The voltage difference in an ionization chamber is only high enough to prevent recombination. When the voltage difference increases to a significantly higher value, from 500 to 1000 V (depending on the geometry), the ionized electrons will gain enough kinetic energy when traveling toward the positive electrode that they will be able to further ionize the atoms, resulting in a single electron avalanche. This effect is called the gas amplification of charge. The amount of charges created in the gas is proportional to the gas amplification factor and therefore to the amount of energy deposited by the incident ionizing particle. Proportional counters can be used to detect and count individual ionizing particles and due to the proportionality between charge and energy, they can discriminate events based on the amount of energy deposited in the detector. To facilitate the movement of electrons between the electrodes, proportional counters are usually filled with a noble gas. The choice of gas depends on the application and the type of particle to be detected (Cherry, Sorenson, and Phelps, 2012b).

2.1.3 Geiger-Müller counters

In contrast to proportional counters, an electron avalanche can trigger another one in a Geiger-Müller counter and the gas amplification effect is increased. The atoms excited from the avalanches return to their ground state very quickly by emitting an ultraviolet (UV) photon. This UV photon can generate a photo-electron by interacting with the gas or even the electrodes. The photo-electron will then excite the atoms as well, continuing the avalanche. This multiplication effect results in a gas amplification factor on the order of 10^{10}, compared to 10^6 for proportional counters. However, the

avalanche results in the same amount of charge, regardless of the energy deposited by the ionizing particle, therefore Geiger-Müller counters are not suitable for energy discrimination (Cherry, Sorenson, and Phelps, 2012b).

Positive ions are much heavier than the electrons, leading to the accumulation of ions close to the negative electrode and reduction of the electric field in the gas, stopping the avalanche. Those positive ions need to be neutralized, but this process can result in the emission of UV radiation that will start another avalanche, without the presence of ionizing radiation. To prevent this, a quenching gas is introduced in the Geiger-Müller counters. This gas usually contains halogen gases such as Cl_2 or organic vapors such as alcohols. The two principal characteristics of a quenching gas are that it can easily lose electrons and that it does not emit UV radiation when it is itself neutralized. Finally, because of their good sensitivity and large signal output, Geiger-Müller counters are used as survey meters in radiation safety (Cherry, Sorenson, and Phelps, 2012b).

2.2 Semiconductor detectors

A semiconductor is essentially a poor electrical conductor and they are used in radiation detection in the same way as gas-filled detectors, but in a solid-state. Semiconducting materials, such as germanium and silicon, are up to 5000 times denser than gas, making them more efficient to stop gamma rays, X rays and charged particles than gas filled detectors. When ionizing radiation creates free electrons in the semiconductor, the charge can be collected by applying an external voltage, similar to ionization chambers. This cannot be achieved with conducting metal, as the charges are already free without the interaction of ionizing radiation. Semiconductor detectors are suitable for single event counting since they only require a deposited energy of 3 to 5 eV to create an ion pair. In addition, the signal is proportional to the energy deposited in the material by the radiation. However, these materials are subject to significant level of

thermal noise and require to be cooled well below the room temperature. Semiconductors are also quite expensive when compared to gas-filled detectors (Cherry, Sorenson, and Phelps, 2012b).

2.3 Scintillation detectors

Scintillators are materials that convert the kinetic energy of charged particles into a light detectable by a photo-detector. This light originates in the electronic transitions from high-energy state to lower energy state. An ideal scintillator must have the following properties. First, the light emitted must be directly proportional to the energy deposited in the materials. Second, the light must be emitted in fast pulses that decay rapidly. Third, the material must have good optical quality and its refraction index around 1.5 to be easily coupled to the photo-detector cathode, which is often made of glass. Finally, the material must be transparent to its emission wavelength, to not absorbs its own signal. Scintillation materials can be divided into two categories: inorganic and organic materials (Knoll, 2000).

2.3.1 Inorganic scintillators

Inorganic scintillators need to be in a crystal shape to produce scintillating light. The crystal requires atoms to be arranged in a specific structure, resulting in discrete energy levels that form a band structure that describes which energies are allowed or forbidden for electrons in the crystal. The lower energy band is called the valence band, and the higher energy band is the conduction band. The energy gap between the valence and the conduction bands is called the forbidden band and electrons are not allowed in this energy band in a pure crystal. To allow electrons to have an intermediate energy, scintillating materials have a small amount of impurities strategically added in the crystal matrix, called activator sites. An electron transiting from the activator site

to the valence band will generate a photon with an energy equal to the difference in energy levels. The impurities are selected so the difference in energy is around two to four eV for a photon in the visible range (Knoll, 2000). A schematic of the scintillation process is shown in figure 2.2 (Lecoq, Korzhik, and Vasiliev, 2014).

1. The absorption of ionizing radiation transfers an electron from the valence to the conduction band, leaving a positive "hole" in the valence band. This combination is called an exciton.

2. The electron-hole pair moves in the crystal, losing energy via collisions.

3. Impurities in the crystal create activator site, also known as luminescence center. The electron can drop to the activator energy level, while the hole will rise the activator ground state.

4. The difference in energy between the activator excited and ground levels is smaller than the energy gap between the conduction and valance bands. Therefore, the electron can recombine with the hole, resulting in the emission of a photon.

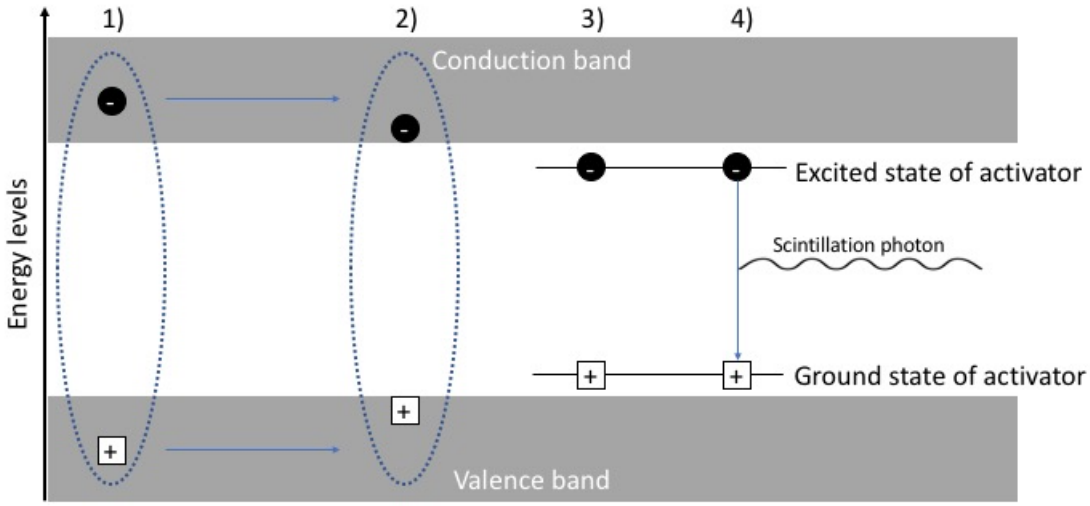

FIGURE 2.2: Schematic of the scintillation process in inorganic crystals. Figure adapted from Lecoq, Korzhik, and Vasiliev, 2014.

Inorganic scintillators typically generate more light than organic for the same amount of radiation, but the process by which light is produce is usually slower. In the second half of the 20th century, inorganic scintillators such as sodium iodide with thallium iodide (NaI(Tl)) impurities and bismuth germanate were used for nuclear imaging modalities. Nowadays, research on inorganic scintillators focuses on developing materials with much faster scintillation time for the fields of nuclear imaging and high energy physics (Knoll, 2000).

2.3.2 Organic scintillators

In contrast to inorganic scintillators, organic scintillators do not need to be in a crystalline matrix to scintillate. Organic scintillators can be solids, liquids or gases, because the emission of light in organic scintillators comes from transitions in the energy levels of a single molecule. As illustrated with the Jablonski diagram in figure 2.3, the ground state for the electron singlet state (spin = 0) is denoted by S_0 and the excited states by S_1 and higher. For the electron in the triplet state (spin = 1), the energy levels are denoted with T. The energy difference between the ground and the first excited states is between two and four eV. The second subscript represents a subdivision of the energy levels, but the differences in energy are so small that transition between subdivisions do not result in emission of light. When ionizing radiation transfers energy to the electrons, electrons will gain energy (represented by upward arrows on figure 2.3) and reach an excited states. Very quickly, on the order of 10^{-12} s, electrons on energy levels higher than S_1 de-excite without emission of radiation to reach the S_1 state. The electrons transition from S_1 to the S_0 state by emitting a photon with energy corresponding to the difference in energy, indicated by downward arrows on figure 2.3. This emission is called fluorescence and is on the order of 10^{-9} s (Knoll, 2000).

Inter-system crossing is the process by which electrons in the singlet state are converted into the triplet state. The triplet state is lower in energy than the singlet, therefore the emitted photons have smaller energies and a different wavelength. This emission is

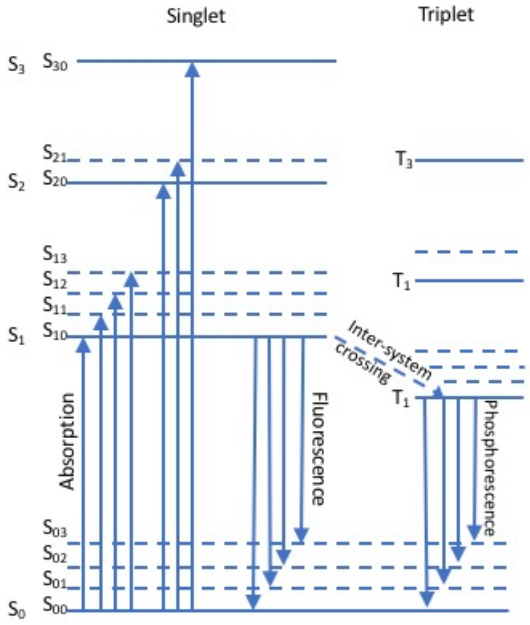

FIGURE 2.3: Transition in energy level for organic scintillation. Figure from Knoll, 2000

called phosphorescence and it is delayed compared to fluorescence, because the lifetime of the T_1 state is on the order of 10^{-3} s. If an electron in the triplet state converts back to the singlet state, the resulting emission spectra will be the same as fluorescence, but on the time scale of phosphorescence. This third emission process is called delayed-fluorescence (Knoll, 2000).

The energy of the fluorescence photons is usually lower than the energy required for the absorption, as displayed by the difference between the upward and downward arrows in figure 2.3. In an ideal case, there is no overlap between the emission and absorption spectra in organic scintillators, but in most cases, there will be an overlap between the two spectra, as shown in figure 2.4.

Another difference between inorganic and organic materials is their densities, which play a role in the total amount of scintillating light produced. Organic scintillators have a much lower density than inorganic, resulting in general in a smaller amount of scintillation light and making organic scintillators less sensitive to photon radiation. The light yield per energy deposited is dictated by the probability of interaction between the ionizing radiation and the scintillating material. Generally, this probability

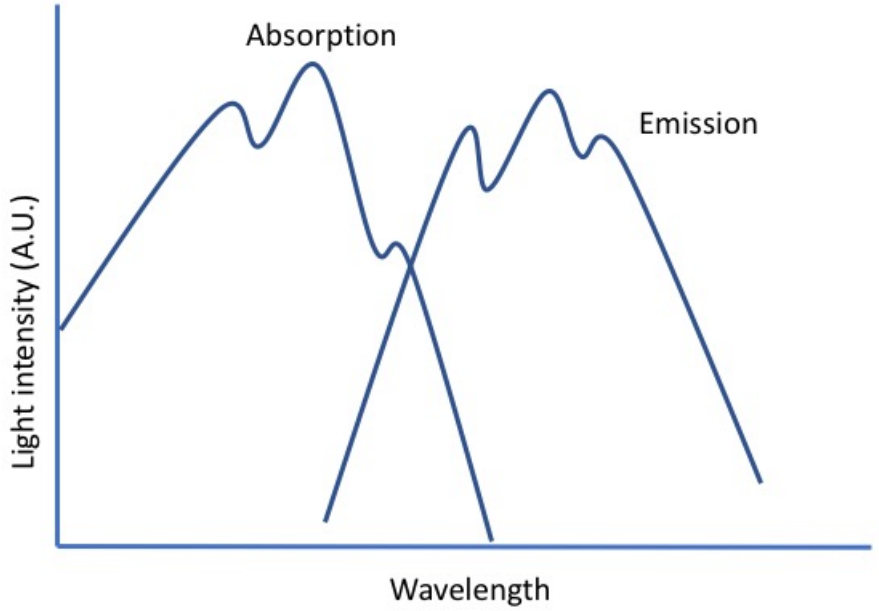

FIGURE 2.4: Absorption and emission spectra as a function of photons' wavelength. Figure from Knoll, 2000

is higher for inorganic scintillators. For example, plastic scintillators generate approximately 8 photons per keV deposited by ionizing particle, while sodium iodide produces 38 photons per keV deposited. Organic scintillators are also cheaper to produce than inorganic crystals and can be produced in many shapes (Knoll, 2000).

2.3.3 Visible light detection

In scintillation detectors, another device must be used to detect the visible photons emitted by the scintillator. Photomultiplier tubes (PMT) convert photons to electrical pulses. The entrance window of a PMT is called the photocathode and converts photons to photoelectrons via the photo-electric effect (section 1.1.4). The photo-electron is accelerated towards a metal plate, called dynode, coated with a material that releases secondary electrons when struck by the photo-electrons. These secondary electrons are accelerated towards another dynode, creating more electrons. There are between 9 and 12 dynodes in a PMT, resulting in a multiplication factor on the order of 10^6. The intensity of the current pulse is proportional to the light signal at the entrance of the PMT,

which is itself proportional to the energy deposited in the scintillator (Knoll, 2000). In addition, a PMT may be replaced in some application by a silicon photo-diode. In contrast to semiconductor radiation detector, photo-diodes detect visible photons from scintillation events, since the photon has enough energy to ionize the silicon and the total charge produced is proportional to the number of incident photons. Photo-diodes can be a lot smaller than PMTs and have a higher detection efficiency, but their gain is equal to one, compared to 10^6 for PMTs, making them less suitable for low signal applications (Cherry, Sorenson, and Phelps, 2012b).

2.3.4 Organic scintillating fibers

Organic scintillators can be fabricated as long optical fibers with thin diameters (a few millimeters). The scintillation light can be transmitted inside the scintillating fiber for distances on the order of meters. Scintillating fibers consist of a core where the scintillation light is produced and one or more thin layers of cladding material to protect the core. The light is transmitted inside the fiber by total internal reflection, which is dictated by Snell-Descartes' law (Knoll, 2000). If the core has an index of refraction $n_1 = 1.6$ and the cladding is $n_2 = 1.5$, the critical angle for total internal reflection is giver by equation 2.1:

$$\theta_c = \arcsin(\frac{n_2}{n_1}) = 69^\circ \tag{2.1}$$

A diagram of the photons being trapped by total internal reflection is presented in figure 2.5. After the emission of scintillating light, photons can exit the fiber or be trapped by total internal reflection if their incident angle is larger than θ_c expressed in equation 2.1. The cladding protects the core from scratches and abrasion, but there is less light trapped in a core-cladding interface than in a core-air interface, because the index of refraction of the cladding is higher than the one for air. Multiclad fibers have more than one cladding layer, with the refractive indices decreasing from the

inner layer to the outer. This increases the amount of light trapped and adds another protection. Scintillating fibers can be operated with a PMT at both ends to measure the light in coincidence, known as a dual readout set-up. If a single readout set-up is used, the end not connected to a PMT will be coated with a mirrored material to reflect as much light as possible back to the measuring device (Knoll, 2000).

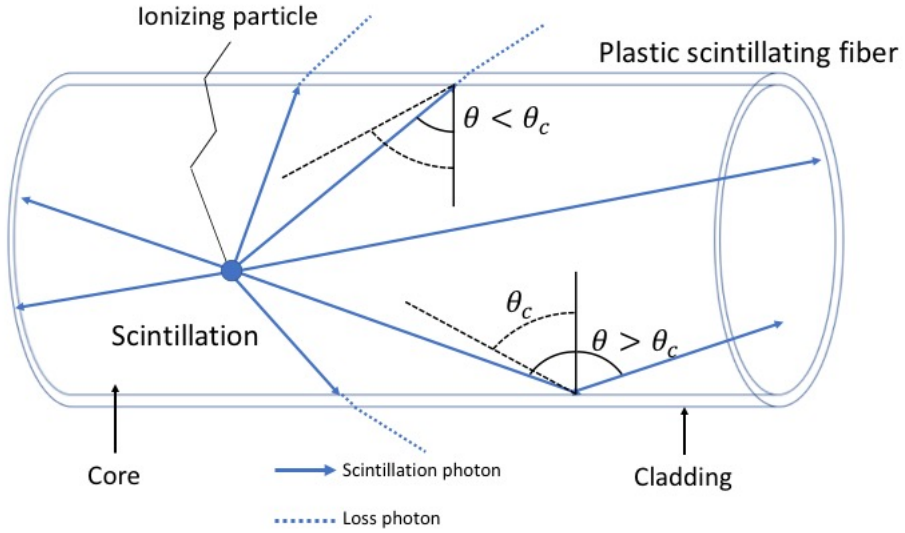

FIGURE 2.5: Schematic of the scintillating photons being transmitted and being trapped in a scintillating fiber.

The attenuation of the scintillation light in the fiber is dictated by several factors, notably: imperfection and the core-cladding interface that change the total internal reflection, scattering inside the core that changes the photon incident angle, making it no longer suitable for total internal reflection and re-absorption because of the overlaps in absorption and emission spectra (figure 2.4). The intensity of the signal $S(x)$ after a distance x from the scintillation site will follow an exponential function represented by equation 2.2, where S_0 is the initial intensity of the signal at the scintillation site and λ_a is the attenuation length (Knoll, 2000).

$$S(x) = S_0 e^{-x/\lambda_a} \tag{2.2}$$

However, in reality, the attenuation as a function of distance does not exactly follow equation 2.2, because the probability of attenuation per path length is not constant.

Figure 2.6 shows graphically the natural logarithm of the ratio $\frac{S(x)}{S_0}$. The attenuation length is shorter at small distances and increases at larger distances. The main reason is the preferred attenuation of shorter wavelengths, i.e. photons of higher energy. The consequence of the preferable absorption of shorter wavelength implies that the average spectrum of light at the end of a long fiber relative to the fiber's attenuation length will be shifted towards the longer wavelengths.

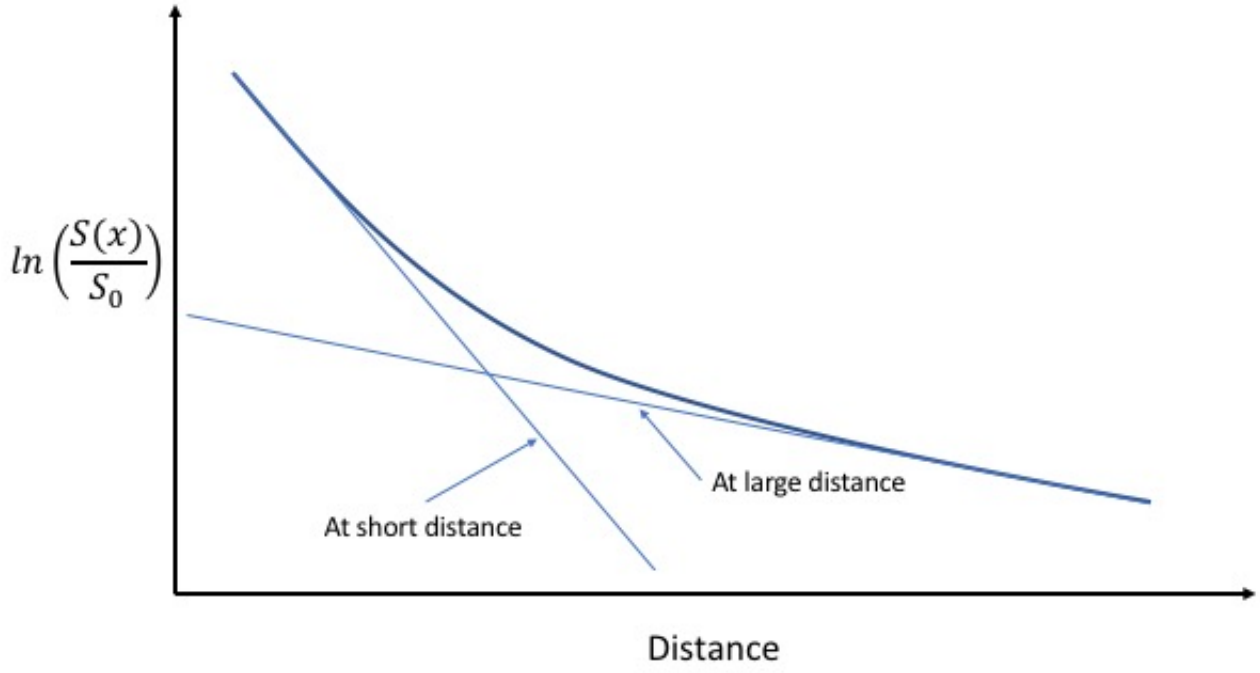

FIGURE 2.6: Natural logarithm of the normalized signal intensity as a function of the distance traveled in the fiber. The attenuation is higher at shorter distance because of the larger attenuation of short wavelength.

Chapter 3

Positron Emission Tomography

Positron emission tomography (PET) is a non-invasive imaging modality used to obtain three dimensional images of organ functions. A solution containing radioactive molecules that can be followed in the organism, is injected in the patient and the scanners records the distribution of the tracer in the patient body. The radioactive molecules are known as radiotracers. This chapter will cover the basics of PET, like the detection mechanism in PET, the different application areas and the acquisition modes.

3.1 PET detection and image formation

The simultaneous emission of collinear photons with an energy precisely equal to 511 keV after the positron annihilation is the most important concept in PET. Due to the energy of the photons, not all photon interactions described in chapter 1 play a role in PET. Compton scattering is the predominant interaction at 511 keV in the patient, but photo-electric effect and Rayleigh scattering are also possible at this energy. PET detectors have a large effective atomic number to increase the probability of photo-electric effect in the detector, increasing the energy resolution. Those detectors are typically inorganic scintillators crystal coupled with PMTs, as described in chapter 2.3.1 and 2.3.3.

When the two photons are simultaneously detected, it is possible to confine their point of emission in the volume defined by the space between the two detectors, as illustrated in the figure 3.1. This volume is called a line of response (LOR). To be considered coincident events, the detectors must record the events within a coincidence time window, which depends on the detector material and the electronics. The coincidence time window is usually between 6 and 12 nanoseconds (Cherry, Sorenson, and Phelps, 2012a).

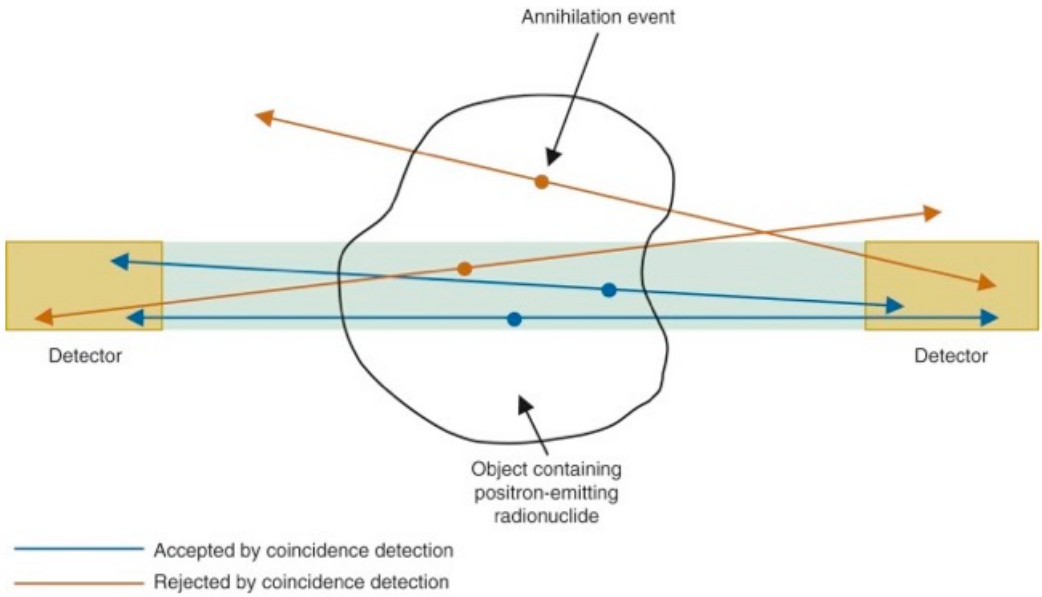

FIGURE 3.1: The detection volume for the two detectors is determined by the shaded area. Both detectors need to record an event during the same coincidence window in order to keep the event. Figure from Cherry, Sorenson, and Phelps, 2012a.

To image a patient inside the scanner, several LOR are formed in the ring of detectors that constitute the PET scanners, as seen in figure 3.2. When detected events are considered to be in coincidence, the energy deposited in the detector is checked against the 511 keV theoretical value. If the energy is lower, it means the detected photon was scattered. The value of the energy threshold is on the order of 75 keV for NaI(Tl) (Cherry, Sorenson, and Phelps, 2012a) and directly affects the spatial resolution. With a higher threshold, more scattered photons are rejected, but the detection sensitivity also decreases. With a lower threshold, the spatial resolution is degraded, but the

sensitivity is increased. NaI(Tl) detectors have an energy resolution on the order of 7%, while Ge(Li) can be as good as 0.4%, because Ge(Li) scintillator generate 33 times more photo-electrons per eV deposited (Cherry, Sorenson, and Phelps, 2012b). There are other factors affecting the spatial resolution in PET. The width of the detector is determined for a compromise between spatial resolution and detection sensitivity. For photons emitted away from the center of the scanner, the width of the detector appears larger because of the detector's thickness. This is known as depth-of-interactions effect and decreases the spatial resolution (Cherry, Sorenson, and Phelps, 2012a). As explained in section 1.3.3, the range of the positron and the non collinearity of the gamma emission also degrade the spatial resolution.

When events meet the criteria of coincidence and energy, the LOR is recorded as a function of its angle and position. The sum of all LOR events is called a sinogram. A reconstruction algorithm is used to convert the sinogram into an image of the radiotracer distribution. The two most common reconstruction algorithms are: filtered back projection and iterative reconstruction. More details on these techniques can be found in Khalil, 2010a.

3.2 PET radiotracers and applications areas

All positron emitting radionuclides are suitable for PET studies. However, to follow a specific function in the body, the radionuclide must radiochemically be attached to a molecule that accomplishes the desired function (Cherry, Sorenson, and Phelps, 2012c). Table 3.1 shows the main radioisotopes used in PET.

Fluorine is not found in the biological system, but its chemical properties allow it to substitute a hydrogen atom or a hydroxyl group, which are common in many biological molecules. ^{18}F is most commonly added to a glucose molecule to form [^{18}F]-fluoro-2-deoxy-2-D-glucose (FDG). It is used in most cancer metabolism studies. When tumor

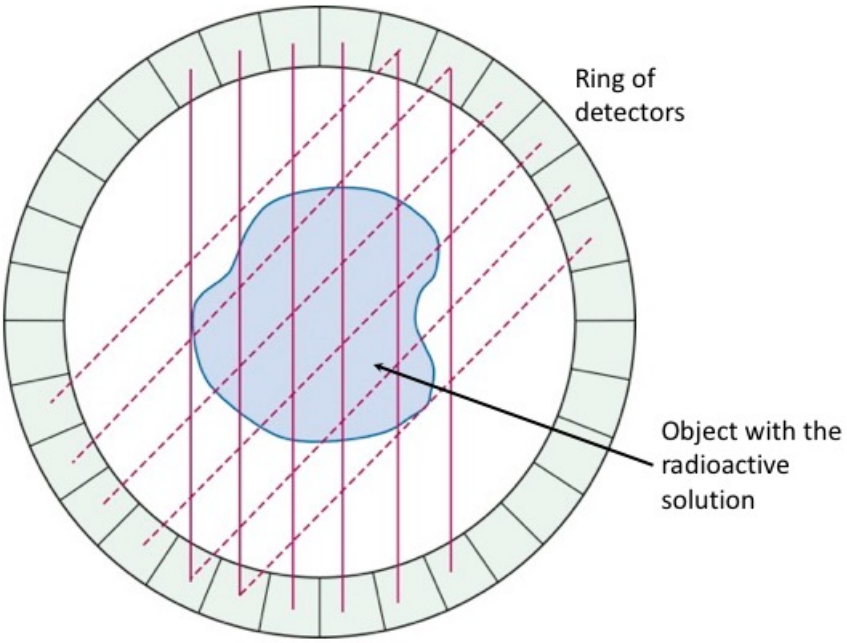

FIGURE 3.2: Ring configuration of a PET scanners with the corresponding LORs between opposing detectors. Note that one detector can have a LOR with multiple detectors. Figure from Cherry, Sorenson, and Phelps, 2012a.

TABLE 3.1: Half-life, mean and maximum values for energy (E_{mean} and E_{max}) and mean and maximum values of range (R_{mean} and R_{max}) in water of commonly used $\beta+$ emitters. Values from Champion and Le Loirec, 2007

Isotopes	Half-life (min)	E_{mean} (keV)	E_{max} (keV)	R_{mean} (mm)	R_{max} (mm)
^{18}F	109.8	252	635	0.66	2.633
^{11}C	20.3	390	970	1.266	4.456
^{13}N	9.97	488	1190	1.730	5.752
^{15}O	2.07	730	1720	2.965	9.132
^{68}Ga	68.1	844	1899	3.559	10.273

cells develop, they have a higher mitotic rate than normal cells and require more energy. Tumor cells prefer the anaerobic pathway to produce their energy in the form of adenosine triphosphate (ATP), leading to an increase in glucose consumption. FDG is actively transported in the cells the same way as regular glucose, but metabolization cycle will stop after phosphorylation and the FDG will accumulate inside the cells as FDG-6-phosphate (Khan et al., 2011). The only way FDG-6-phosphate can exit the cell is if it recombines back to FDG, but this only occurs after roughly 1.5 hours, which is longer than most FDG scans. Even if the glucose molecule is phosphorylated before the ^{18}F atom decayed, the emission of positron will occur inside the cell since the ^{18}F

atom is trapped inside (Bentourkia, 2010).

Carbon, nitrogen and oxygen are key components of biological systems. ^{11}C-methionine, a marker of amino acid uptake, is used in oncology since most brain tumors show an increase in protein synthesis and amino acid uptake (Derlon et al., 1989; Weber et al., 2000). ^{13}N-ammonia is used in cardiology applications, as it is a tracer for myocardial blood flow. Its fixation in the myocardium is a metabolic pathway, and changes in hemodynamics of the heart will alter the uptake of ^{13}N-ammonia (Schelbert et al., 1981). ^{15}O can be added to a water molecule and the resulting $H_2{}^{15}O$ molecule can be injected as a freely diffusing radiotracer to assess cerebral or tumor blood flow (Mintun et al., 1984).

Finally, ^{68}Ga has the advantage that its production does not require a cyclotron. It can be extracted from a ^{68}Ge-^{68}Ga generator, the same way as ^{99m}Tc (Hnatowich, 1977). ^{68}Ga is an interesting positron emitter not only due to its simpler production method, but also for its chemical properties. For example, it can be used to label prostate-specific membrane antigens, which have increased expression on prostate cancer cells (Afshar-Oromieh et al., 2013).

3.3 Acquisition modes for PET

3.3.1 Static acquisitions

A PET scan acquisition can be either static or dynamic. In a static scan, the distribution of the tracer is recorded over the entire length of the scan, resulting in a single image frame at the end. Static scans are usually performed for cancer diagnostic and staging, based on the relative tracer uptake (Muzi et al., 2012). To characterize the relative tracer uptake, the standardized uptake value (SUV) is used. SUV is a semi quantitative value due to its lack of units and it is calculated as (Thie, 2004):

$$\text{SUV} = \frac{C_{PET}}{D/w} \tag{3.1}$$

In this equation, C_{PET} is the mean intensity in the region of interest (ROI) on the PET image (in Bq/kg) corrected for radioactive decay, D is the total dose injected (in Bq) and w is the weight of the patient (in kg). The advantage of the SUV is that it is a fast and simple method. On the other hand, it does not account for the different distribution between tissue and fat, nor partial volume and spillover effect (Khalil, 2010b) in the ROI. Moreover, there is no distinction between blood and tissue in the ROI. Finally, when using the SUV, the concentration of the tracer is approximated to be in a steady state over the entire time of the scan. This approximation is not realistic, which adds uncertainties in C_{PET} (Bentourkia, 2010).

3.3.2 Dynamic acquisitions

When data for the same volume are obtained for different time intervals, the scan is considered dynamic. The result of the scan is a movie that follows the radiotracers distribution for the entire length of the scan. The advantages of dynamic scans include a better assessment of the tracer uptake throughout the scan and the possibility to extract quantitative information on the biological process studied with the tracer. The biological process can be the determination of the cerebral blood flow, the assessment of tumor perfusion or the measurement of absolute glucose metabolism. With dynamic scans, the value of the activity concentration in a voxel or a ROI at each time frame is obtained. A typical timing sequence for a dynamic PET study with ^{18}F is: fifteen 5 s acquisitions, five 15 s, five 30 s, four 60 s, four 3 minutes and finally nine 5 minutes acquisitions (Muzi et al., 2012). Because of the relatively short half-life of ^{18}F, short acquisitions at the beginning will have a similar signal-to-noise ratio (SNR) than longer acquisitions towards the end. Plotting the activity concentration as a function of time

results in time-activity curves (TAC). Figure 3.3 shows an example of the TAC from different regions in the brain (Erlandsson, 2010).

One of the most popular methods to obtain quantitative information from the TAC is to use a mathematical model to describe the variations in the TAC. Most models consist of a compartmental analysis where the different compartments represents different regions, such as the vascular compartment, the extracellular space compartment or the intracellular compartment. The earlier models were described by Carson (1991). This type of analysis is called pharmacokinetic modeling. The following chapter will describe how the TAC is analyzed within the compartmental model and how the results of this analysis are related to the previously mentioned biological processes.

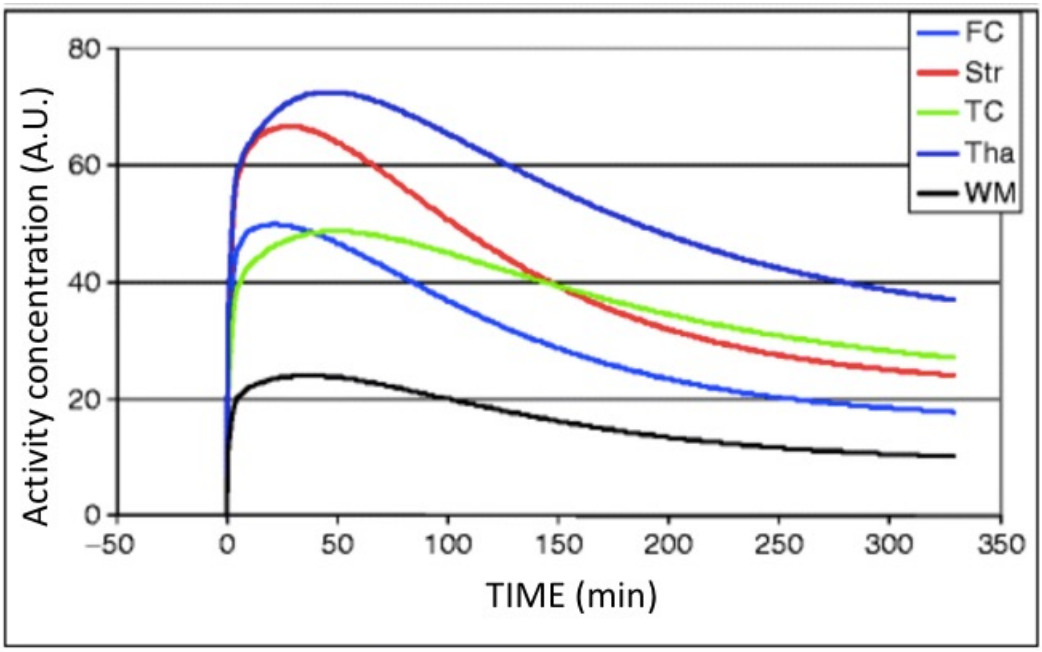

FIGURE 3.3: Time-activity curves (TAC) for different regions of the brain: Frontal cortex (FC), striatum (Str), temporal cortex (TC), thalamus (Tha) and white matter (WM). Figure from Erlandsson, 2010.

Chapter 4

Pharmacokinetic modeling

4.1 The compartmental model

This type of pharmacokinetic model assumes the radiotracers in the body are in distinct compartments. Figure 4.1 represents a basic three compartment model. The rate at which the concentration changes in a compartment is proportional to the concentration in the neighboring compartments and a first order rate constant. Mathematically, it can be represented by differential equations as:

$$\frac{d}{dt}C_i(t) = \sum_{j=1}^{N}[k_{ij} \cdot C_j(t) - k_{ji} \cdot C_i(t)] \tag{4.1}$$

In equation 4.1, C_i is the concentration of the radiotracers in the compartment i, N is the total number of compartments in the model and k_{ij} is the transfer constant from compartment j to compartment i. The rate constants are denoted with a single index and have units of min^{-1}, except for the blood-to-tissue rate constant, known as the clearing term, which is in units of blood flow: mL of blood or plasma per minute per mL of tissue. These models are solved using the Laplace transform method (Erlandsson, 2010). As an example, the three compartments model for FDG pharmacokinetics analysis developed by Phelps et al., 1979 is described below. Figure 4.1 shows schematically the transfer of FDG molecules through the compartments. Based on equation 4.1,

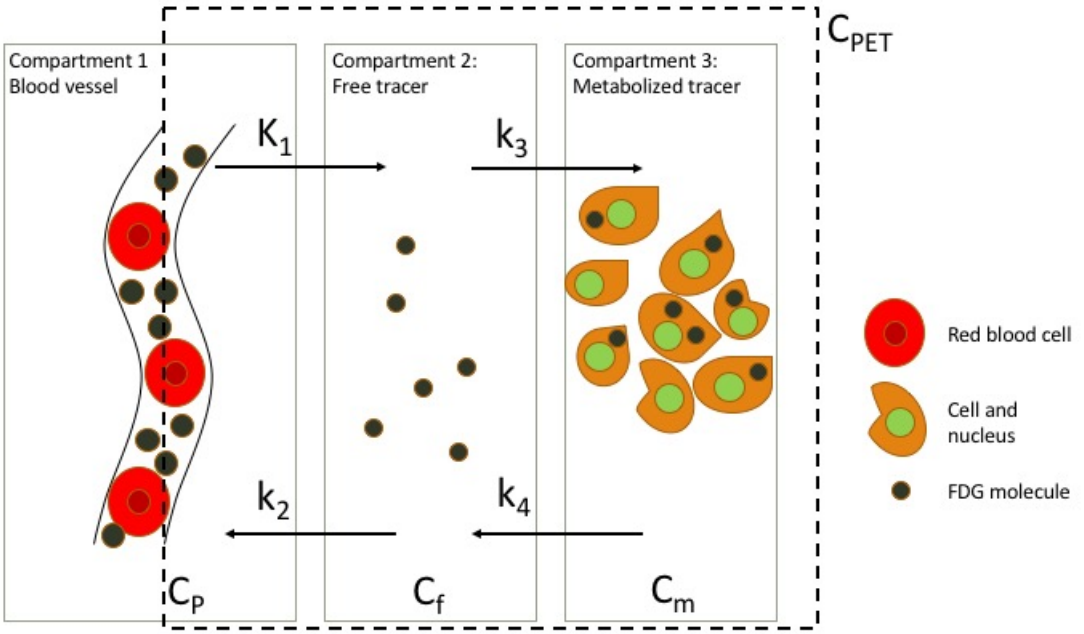

FIGURE 4.1: Schematic of a three compartment model. The concentration of radiotracers (black dots) in each is dictated by the transfer rate constant K_1 to k_4 in this case. C_P is the concentration in the plasma, C_f is the free FDG concentration and C_m is the metabolized FDG concentration. C_{PET} is the concentration given by the PET image.

the rate of change for the free (C_f) and the metabolized (C_m) compartments are:

$$\frac{d}{dt}C_f(t) = K_1C_P(t) - (k_2 + k_3)C_f(t) + k_4C_m(t) \tag{4.2}$$

$$\frac{d}{dt}C_m(t) = k_3C_f(t) - k_4C_m(t) \tag{4.3}$$

The equations 4.2 and 4.3 are solved using the Laplace transform (more details in Erlandsson, 2010). The following solutions are obtained:

$$C_f(t) = \frac{K_1}{\alpha_2 - \alpha_1}[(k_4 - \alpha_1)e^{-\alpha_1 t} + (\alpha_2 - k_4)e^{-\alpha_2 t}] \bigotimes C_P(t) \tag{4.4}$$

$$C_m(t) = \frac{K_1k_3}{\alpha_2 - \alpha_1}(e^{-\alpha_1 t} - e^{-\alpha_2 t}) \bigotimes C_P(t) \tag{4.5}$$

Where the $\otimes$ symbol represents a convolution and C_P is the concentration of radiotracers in the plasma in the case of FDG modeling. The constants α_1 and α_2 are combinations of k_2, k_3 and k_4 defined as:

$$\alpha_1 = \frac{k_2 + k_3 + k_4 - \sqrt{(k_2 + k_3 + k_4)^2 - 4k_2k_4}}{2} \tag{4.6}$$

$$\alpha_2 = \frac{k_2 + k_3 + k_4 + \sqrt{(k_2 + k_3 + k_4)^2 - 4k_2k_4}}{2} \tag{4.7}$$

As depicted in figure 4.1, the results from the PET images is C_{PET}, which is the sum of C_f, C_m and an unknown fraction of C_P. This fraction of blood vessel is called the tissue vascular fraction and is denoted by a fifth constant, k_5, a unit less number. C_{PET} can therefore be expressed as:

$$C_{PET} = \frac{K_1}{\alpha_2 - \alpha_1}[(k_3 + k_4 - \alpha_1)e^{-\alpha_1 t} + (\alpha_2 - k_3 - k_4)e^{-\alpha_2 t}] \bigotimes C_P(t) + k_5 C_P(t) \tag{4.8}$$

A summary of the elements needed to perform a pharmacokinetic analysis on PET images are shown in figure 4.2. Equation 4.8 constitute a problem with essentially three variables. C_{PET} is obtained from the PET images and the transfer rate constants "k" are obtained from a least-square fitting algorithm of equation 4.8. Therefore, C_P, known as the arterial input function (AIF) must be obtained prior to the mathematical analysis.

4.2 Arterial input function

The AIF is either the concentration of the radiotracer in the whole blood (such as $H_2{}^{15}O$) or in the plasma (such as FDG). The clinical standard to determine the AIF

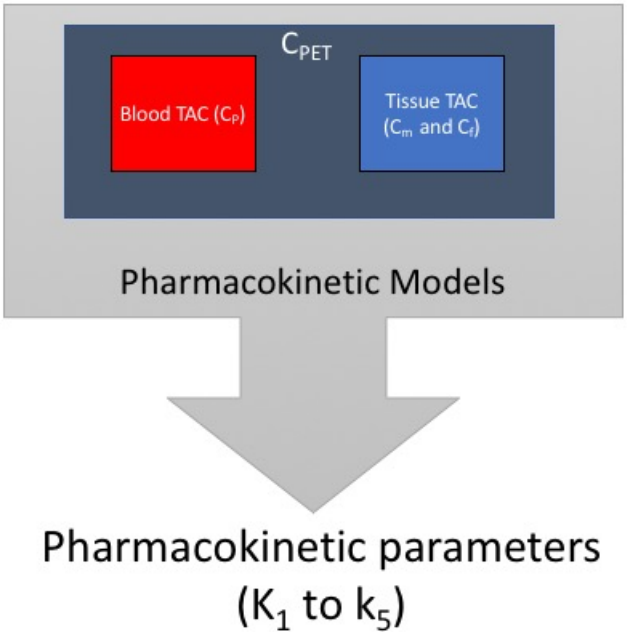

FIGURE 4.2: Diagram showing the data needed to do pharmacokinetic analysis on PET images. The pharmacokinetic parameters are obtained from a pharmacokinetic model applied to the blood TAC and the tissue TAC. The two TACs are both present in the PET image under C_{PET}.

is to acquire blood samples through invasive manual or automatic blood sampling methods during the PET scan. Manual blood sampling consists in withdrawing blood at different time points from an artery or a vein and then further analyze the samples to obtain the activity and the tracer concentration. Just as the dynamic images (see section 3.3.2), more blood samples are acquired at the beginning of the scan. However, this comes with several disadvantages including: important discomfort to the patient with the risk of hematoma, swelling and thrombosis (Jons et al., 1997), the risk of exposing the medical staff to diseases and ionizing radiation as well as the risk of radioactive contamination. Additionally, unless the blood sampling rate is very high, delays and dispersion in the measured activity versus the true activity are expected. A more precise description of the technique can be found in Greuter et al., 2003. To simplify the blood sampling workflow, automated sampling was introduced. The blood from an artery is continuously pumped through a catheter that passes through a radiation counter, measuring directly the activity. Despite reducing the risk of exposing the medical personnel to potentially significant radiation dose, automatic sampling will

always have contamination from the previous blood and this introduces a dispersion of the AIF that is not a representation of the reality. In addition, due to the catheter length, there is a difference between the arrival of the blood in the detector and in the tissues. Detailed information on automated blood sampling techniques are given by Boellaard et al., 2001. Figure 4.3 shows the steps and the equipment needed when sampling blood manually and with an automated system. Consequently, alternative non-invasive sampling approaches are being considered to determine the AIF in a way that would reduce patient discomfort, lower the risks presented to the personnel, and aid in calculating the kinetic information from a PET scan.

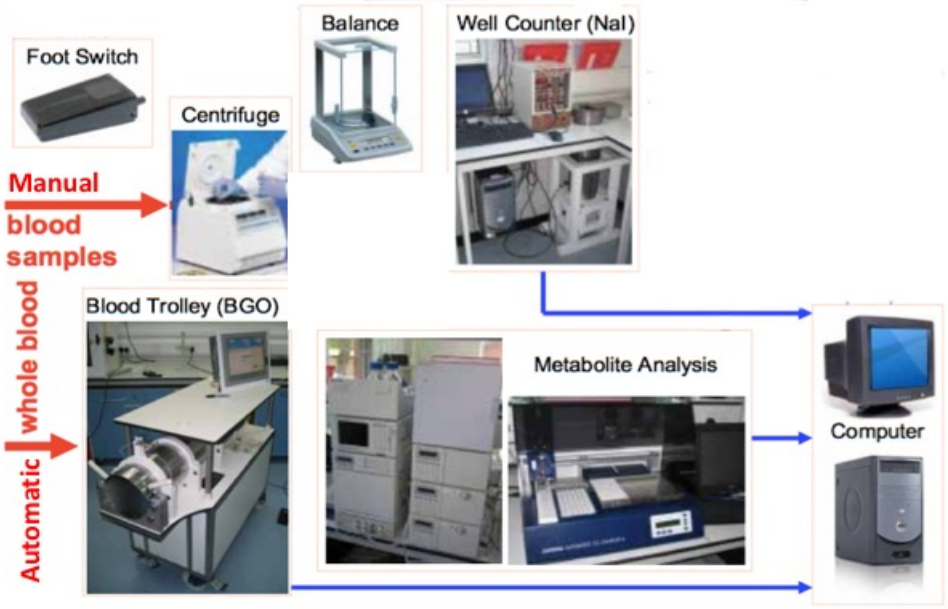

FIGURE 4.3: Work flow and equipment needed for manual and automated blood sampling to obtain the AIF. Figure taken from the University of Manchester Wolfson Molecular Imaging Center

4.3 Current non-invasive techniques

A simple way to obtain the AIF would be to directly use a region filled with blood on the PET images, for example the left ventricle or a large artery such as the aorta (Feng et al., 1997). This method eliminates the need for blood sampling and calibration

of the samples' radioactivity. But due to the poor spatial resolution available in PET, partial volume effect and spillover (Khalil, 2010b) will introduce errors in the AIF (Lin et al., 1995). Also, the timing resolution is determined by the acquisition time of each frame, which needs to be long to collect enough annihilation photons and is too slow to accurately represent the AIF's peak. In addition, a study by Zanotti-Fregonara et al., 2009 on FDG concluded that none of the eight methods used to obtain the image-derived input functions provided a reliable quantification of cerebral metabolic rates of glucose. Finally, for this technique to work, the heart or large enough arteries must be in the FOV, which is not always possible, especially in brain studies.

Another method consists in using a population based AIF, derived from previous blood samples from many patients (Takikawa et al., 1993). For individual patients, this general AIF is normalized with one blood sample. The main drawbacks of this technique are the omission of biological differences between patients and the obligation to perform all PET scans under similar conditions and protocols.

Several research groups have developed detectors to measure the AIF non-invasively.. Litton and Eriksson, 1990 developed a transcutaneous detector placed on the surface of the skin over the carotid artery. Watabe et al., 1995 placed two plastic scintillators on the wrist, one over the radial artery to record the AIF and one over tissue to measure the background radioactivity that would be subtracted from the AIF. Yamamoto et al., 1999 used a beta camera placed over the radial artery to obtain the AIF from the images taken by the camera. The same group then worked on a tweezer detector based on a pair of inorganic scintillators (LSO crystals) recording coincidence counts, coupled to optical fibers (Yamamoto et al., 2005). Villanueva et al., 2003 used a wrist detector similar to Watabe et al., 1995, but used LSO crystals to detect annihilation photons and have enough signal to extract the AIF from image derived input function techniques. Pain et al. 2000; 2002; 2004 developed a β^+ micro probe for measurements in animals. The probe consists of a small piece of scintillating fiber, coupled to a clear optical fiber

and could be inserted in a region of the rat's brain to monitor directly the radioactivity, without the need of a small animal PET scanner. The probe could also be placed in the rat's femoral artery and measure the AIF directly. A second probe needed to be placed on the skin's surface next to the artery to account for background radiation from annihilation photons. This group also used Monte Carlo simulations to calculate the effective volume of detection of their probe and discovered that the orientation and the position of the probe inside the artery affected the measured AIF. Kriplani et al., 2006 developed a wrist scanner based on LSO crystals, that could distinguish between arterial and venous signal on the images it acquired. Lee et al., 2008 improved the design from Pain et al. to make it useful in the human arm by eliminating the clear fiber and coupling the scintillating fiber directly to a PMT. In addition, an algorithm was developed allowing them to remove the second probe used to subtract the background from the AIF measurements. The drawback with most of the detectors presented above is the significant undesirable signal of positrons coming from the veins and surrounding tissues as well as annihilation photons coming from the entire body, resulting in a low SNR (Feng et al., 1997).

4.4 Objectives

The aim of this project was to develop and characterize a cost-effective and non-invasive alternative for measuring the AIF using scintillating fibers for positron detection. The detector will be placed on the wrist of the patient in a spaced curved pattern, for example an S-shaped pattern or circular loops similar to wristlets, and subsequently measure the AIF through detection of emitted positrons passing through the radial and ulnar arteries. Ideally, the detector would be independent of, but compatible with PET and PET/MRI (magnetic resonance imaging) and will also be portable. The detector will also distinguish the arterial signal and the background coming from veins and

surrounding tissues, which will improve the AIF measurement. If successful, this detector would provide accurate AIF measurements and eliminate the discomfort felt by the patient as well as the hazards faced by the personnel.

Nowadays, dynamic PET imaging is almost exclusively used as a research tool, partially due to all the requirements for determining the AIF. A non-invasive detector that provides an AIF at least as good as invasive blood sampling will allow more centers to perform dynamic imaging in a clinical setting as well as decrease the ethical burden on clinical trials.

Chapter 5

Methodology

5.1 Detector set-up

Figure 5.1 is a representation of the prototype dual readout set-up. The scintillating fiber, with a core of polystyrene (BCF-12, Saint-Gobain), is covered by a black protective tubing (7.2 μm thick, Vention Medical). Scintillating fibers emit light when they absorb energy from ionizing radiation. In BCF-12, the emission spectrum ranges from 385 nm to 5575 nm, with a peak emission at 435 nm. The scintillating fiber is coupled at both ends to a 11 meter transmission fiber with a core of PMMA (Eska, Mitsubishi). Table 5.1 lists several properties for the scintillating and transmission fibers. Each end of the transmission fibers is connected to a PMT (H6779, Hamamatsu) and the PMTs' outputs are monitored simultaneously with an oscilloscope (DSO-X 2012A, Keysight) without amplification. The oscilloscope signal is recorded with an instrument driver directly in Matlab.

When the radioactive tracers are passing through the radial and ulnar arteries, a percentage of their emitted positrons will be able to exit the patient and reach the detector, as the maximum range of positrons used in PET (table 3.1) is larger than the depth of the radial artery (average of 1.99 $\pm$ 0.99 mm (Lee et al., 2016)). When the positron interacts with the scintillating fiber, scintillating photons are emitted isotropically and

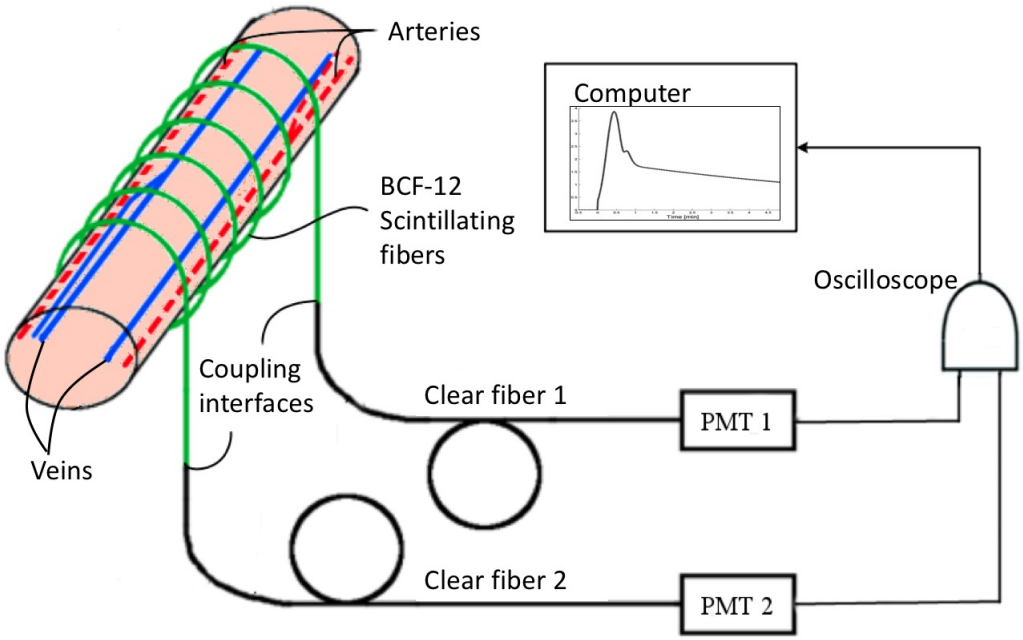

FIGURE 5.1: Schematic representation of the dual readout detector.

travel toward the PMT. The total number of photons detected with the PMT will depend on its quantum efficiency, the coupling efficiency between the transmission fiber and the scintillating fiber, the fraction of scintillating photons that are trapped by total internal reflection in the BCF-12 fiber and finally, on the attenuation in both fibers (Beddar et al., 2003; Archambault et al., 2005).

5.2 Attenuation measurements

Since the emission and absorption spectra of plastic scintillating fibers overlap (Knoll, 2000), it is necessary to measure the attenuation of the light signal as a function of distance traveled in the scintillating fiber. A 2.5 cm radius ^{137}Cs (186.5 kBq) gamma source was positioned each 10 cm along the fiber axis. For each position, ten 5 ms waveforms with a sampling rate of 12.5 MHz were acquired with the oscilloscope. Each waveform is integrated, and the individual sums are then averaged. To account for the background level, ten measurements without the source were made and the average background level subtracted to the signal. These measurements were first

TABLE 5.1: Properties of scintillating and transmission fibers. Data obtained from the Saint-Gobain and ESKA.

Characteristic	**BCF-12**	**Eska GH4001**
Core material	Polystyrene	PMMA
Core density	1.05 $\mathrm{g/cm^3}$	1.2 $\mathrm{g/cm^3}$
Core refractive index	1.60	1.49
Cladding material	PMMA	Fluorinated Polymer
Cladding refractive index	1.49	N/A
Diameter, with cladding	1.00 $\pm$ 0.02 mm	1.000 mm
Numerical aperture	0.74	0.5
1/e attenuation length	270 cm	5101 cm
Emission peak	435 nm	-
Scintillation decay time	3.2 ns	-
# of photons / MeV	$\approx$ 8000	-

done in a similar manner as Saint-Gobain does to test their fibers (Saint-Gobain, 2005). A 3.0 m long scintillating fiber directly coupled to a PMT in a single readout set-up was excited with the ^{137}Cs source at distances between 1 to 3 m. The attenuation of the signal was modeled with an exponential function (Knoll, 2000):

$$S_1 = A \cdot e^{-x/\lambda_a} \tag{5.1}$$

Where S_1 is the PMT signal, x is the position of the ^{137}Cs source, λ_a is the 1/e attenuation length of the scintillating fiber and A is a normalization constant.

For the dual readout set-up, two detectors were tested, one with a 1.5 m scintillating fiber and the second with a 3.0 m scintillating fiber. The gain of each PMT needs to be adjusted to obtain approximately an equal output for an excitation at the center position on the scintillating fiber. To eliminate the possible differences in the excitation source intensity between each point, the ratio of the output at each PMT was used. The ratios where normalize to be 1 at the center position. The ratio of the PMTs' output (S_1/S_2) should follow a decreasing mono exponential with the form:

$$\frac{S_1}{S_2} = e^{-2x/\lambda_a} \tag{5.2}$$

In equation 5.2, x is the position of the ^{137}Cs source with $x = 0$ at the center of the fiber and λ_a is the 1/e attenuation length of the scintillating fiber. Because the scintillation light generated by the ^{137}Cs source is weak, this measurement was also performed with a UV lamp (36 W), which produced a much larger and constant light signal.

5.3 Bending losses

As shown in figure 5.1, the scintillating fiber is wrapped around the patient's wrist to increase the detection area. Bending the fiber can change its shape and reduce the detector efficiency (Chung and Margulies, 1995b). To evaluate this, the difference in output at each PMT was measured for a fixed excitation point at one end of the scintillating fiber and different loop diameters in the fiber, as shown in figure 5.2. Because of the finite length of the scintillating fiber in the detector and to make sure the excitation source did not introduce signal inside the loop, there was only one loop for each measurement. The signal was acquired in the same way as described in the previous section. The measurements were also made with the UV source. The losses L were calculated as:

$$L = \frac{R_0 - R}{R_0} \cdot 100 \tag{5.3}$$

Where R_0 is the ratio of the output at PMT_2 over the output at PMT_1 when the fiber is straight and R is the same ratio for different bending radii of the scintillating fiber.

5.4 Phantom measurements

In a clinical situation, the detector must be able to detect the positrons from a PET radionuclide. To simulate a clinical scenario, a cylindrical wrist phantom (diameter of 64.1 mm and height of 64.8 mm) made of polyethylene (density: 0.94 $\mathrm{g/cm^3}$) , with

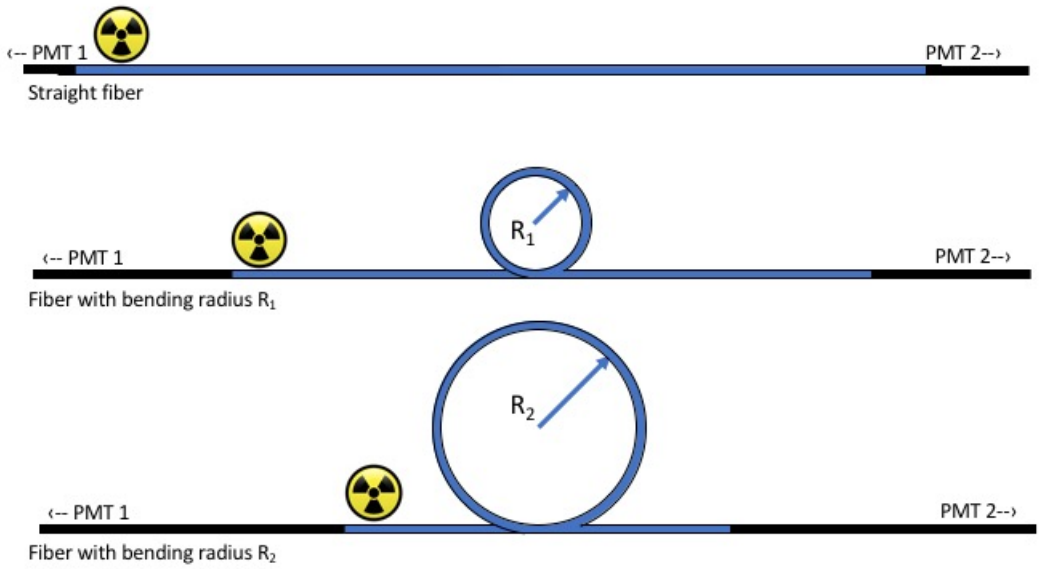

FIGURE 5.2: Set-up for the bending losses measurement. The total length of the scintillating fiber (blue) is constant for each loop. The position of the excitation source is also kept constant.

holes drilled in it to mimic blood vessels, was built. The holes have a diameter of 3.25 mm and sit at a depth of 2 mm. The dimensions were verified with transverse MRI images of the wrist. Polyethylene and soft tissue have similar attenuation coefficients for 500 keV photons, with 0.106 cm^{-1} and 0.096 cm^{-1} respectively (Hubbell and Seltzer, 1996) and similar stopping power for positrons in the range of energy relevant to PET (Berger and Seltzer, 1983). The scintillating part of the detector was wrapped five times around the phantom.

A 1.5 m long plastic tube was used to mimic a blood vessel and was positioned in a manner to have the radioactive solution passing through the phantom and exit into a waste bottle that was shielded as shown on figure 5.3. The two radionuclides available for this study are ^{18}F and ^{11}C. The radioactivity concentration for their solution was respectively 7.4 MBq/ml and 3.7 MBq/ml. Their half-life, the maximum and mean positron energy and range in water are displayed in table 3.1. The longer range of

positrons from ^{11}C makes it a good subject for the detector and ^{18}F is the most commonly used radionuclide in PET. The radioactive solutions are injected as a pulse inside the phantom to mimic the first passage of the input function in the arteries. The response of the detector is monitored with the oscilloscope recording 5 ms waveforms with a rate of 2.87 waveforms per second. The signal from each waveform is integrated over the entire 5 ms. The acquisition for the ^{18}F solution lasted 4 minutes and 15 seconds and the ^{11}C lasted 1 minute and 56 seconds. The background level was subtracted from the signal as described previously.

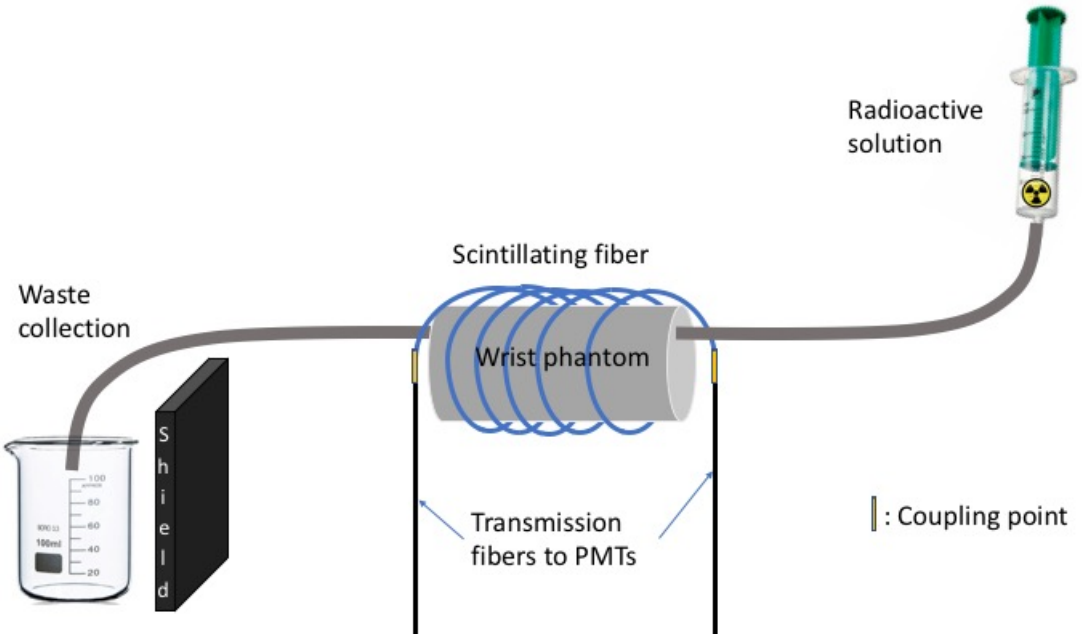

FIGURE 5.3: Representation of the phantom with a tube imitating a blood vessel. The radioactive solution is injected through the tube and collected in a waste recipient shielded from the detector.

In addition to the simple input function, the response to different levels of radioactivity is measured with the solution of ^{11}C. Its 20.3 min half-life makes it a good candidate to measure its decay over a relatively short period of time. 3.02 MBq of ^{11}C were inserted inside the phantom and a 5 ms waveform was acquired every 1.4 seconds for a total time of 1 hour, 24 minutes and 31 seconds. The decay constant for ^{11}C was extracted from an exponential fit of the data with Matlab.

Chapter 6

Results

6.1 Attenuation measurements

Figure 6.1 displays the intensity of the PMT output for the single readout scintillating fiber excited by the ^{137}Cs source. The black squares are the average of the 30 measurements at each position of the source. The vertical lines represent the standard error on the mean of the 10 measurements. The solid lines are the boundaries defined by the root mean square error (RMSE) on the fit of equation 5.1. The attenuation length obtained from the fit of the data is 278 $\pm$ 49 cm. The dashed curve in figure 6.1 is equation 5.1, with λ_a = 270 cm, which is the attenuation length specified by Saint-Gobain, and A = 1954, the same normalization constant as the experimental data.

Figure 6.2 shows the attenuation length measurements for the 3.0 m detector with the ^{137}Cs (figure 6.2-A) and UV source (figure 6.2-C). Figure 6.2-B and figure 6.2-D are also the ^{137}Cs and UV source excitations respectively, but for the 1.5 m detector. The legend is the same for each panel. The ratio PMT_1 over PMT_2 is displayed in red, and the inverse in blue. The filled circles are the average of 10 measurements done at each position. The vertical lines are the uncertainties for the 10 measurements, calculated using the quadratic sum of the relative uncertainties on each PMT output (Taylor, 1997). The uncertainties do not show on the UV measurements, as they are too small. The dashed curves are exponential curves from equation 5.2 with λ_a = 270 cm, the attenuation

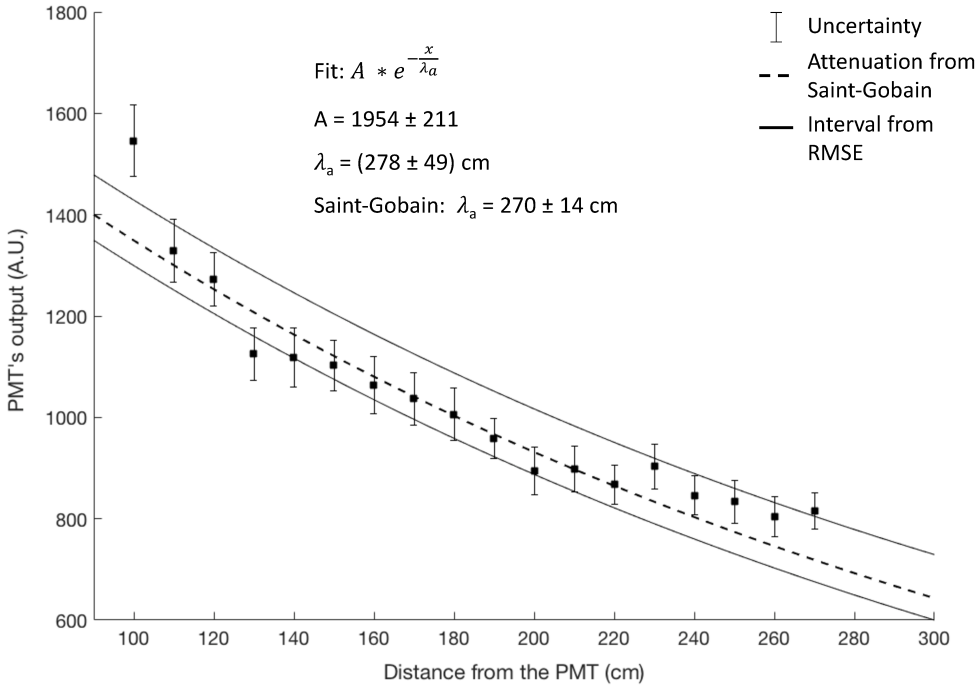

FIGURE 6.1: Single readout attenuation measurement with the ^{137}Cs source. The black squares are the experimental data, with the vertical lines being the standard deviation of each measurement. The solid curves represent the uncertainty on the data fits. The dashed curve is the attenuation specified by Saint-Gobain.

length specified by Saint-Gobain. Finally, the solid curves are the boundaries of the root mean square error on the fit of equation 5.2 on the data. The attenuation lengths obtained from the ^{137}Cs measurements are 277 $\pm$ 12 cm and 261 $\pm$ 16 cm for the 3.0 m and the 1.5 m detector, respectively. With the UV source, the attenuation length are 307 $\pm$ 6 cm and 294 $\pm$ 8 cm, again for the 3.0 m and 1.5 m respectively. The uncertainty on the attenuation lengths comes from the 95 $\%$ confidence interval on the fit parameters provided by Matlab (R2017a).

6.2 Bending losses

The bending losses calculated from equation 5.3 are shown in table 6.1. The uncertainty on the bending losses for the ^{137}Cs measurements were larger than the measured losses for every radius. However, with the UV measurements, the uncertainties on the losses

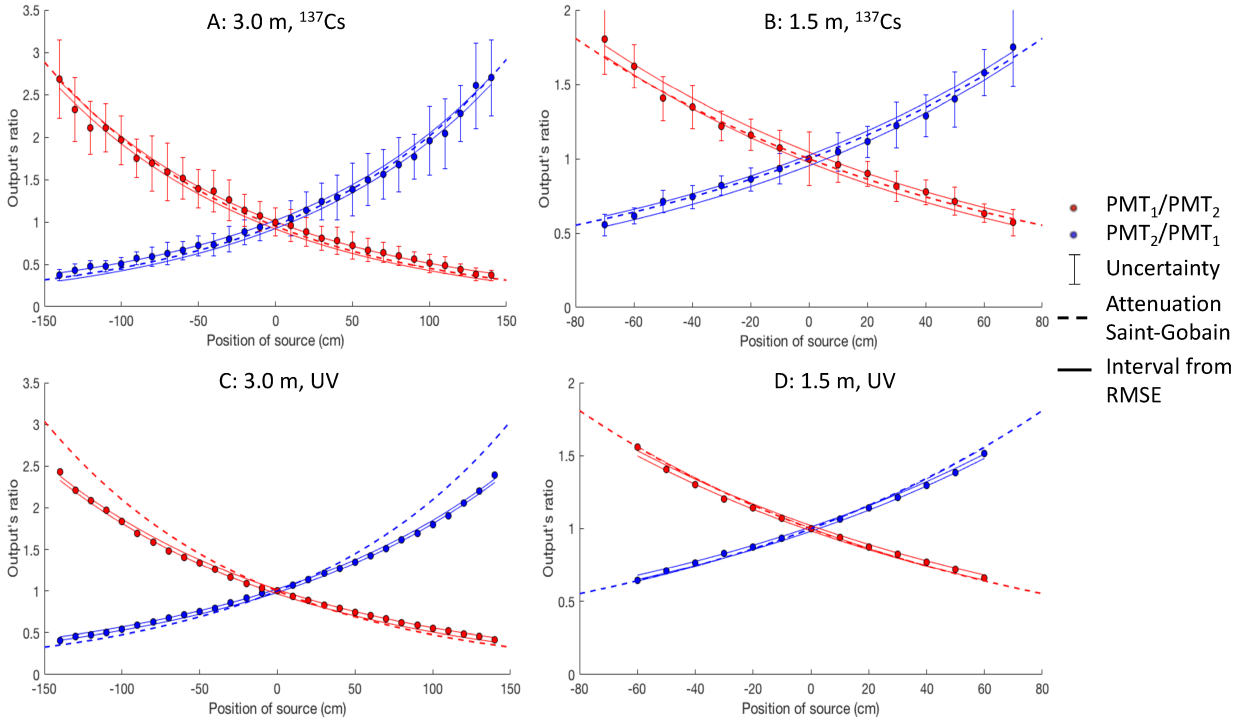

FIGURE 6.2: Attenuation length measurements for the 3.0 m detector, with the ^{137}Cs source and the UV source (A and C respectively). B and D are the attenuation length measurements with the with the ^{137}Cs source and the UV source, but for the 1.5 m detector.

percentage are on the order of 0.0002%. The very small uncertainty allows to see that the losses increase linearly as the bending radius decreases.

TABLE 6.1: Losses (in percent) from equation 5.3 for different bending radii compared to a straight fiber. UV uncertainties ≈ 0.0002%.

	Scintillating fiber bending radius (cm)						
	15.0	13.5	12.0	10.5	9.0	7.5	6.0
UV	0.82	0.87	1.13	1.45	1.59	1.72	2.20
^{137}Cs	3.1±5.4	3.0±6.8	3.4±6.5	4.4±7.8	2.8±6.3	2.1±6.3	4.5±5.7

6.3 Phantom measurements

Both first pass input function measurements are displayed in figure 6.3-A for ^{18}F and figure 6.3-B for ^{11}C. The red curves represent the integrated signal of the 5 ms waveforms acquired with the oscilloscope. The black curves are the smoothed versions of

the red curves, obtained from a moving average of 5 points. Both figures are normalized to 100 at the highest point. The top part of the ^{18}F step function starts after 32 seconds and the injection lasts 36 seconds. The top part for the ^{11}C step function rises at the 30 seconds' mark and the injection lasts 26 seconds. The SNR was taken by dividing the mean of top part of the step function divided by the standard deviation of the bottom part of the step function, as defined in T. Bushberg et al., 2011. The SNR is 21.29 and 29.40 for the ^{18}F and ^{11}C respectively.

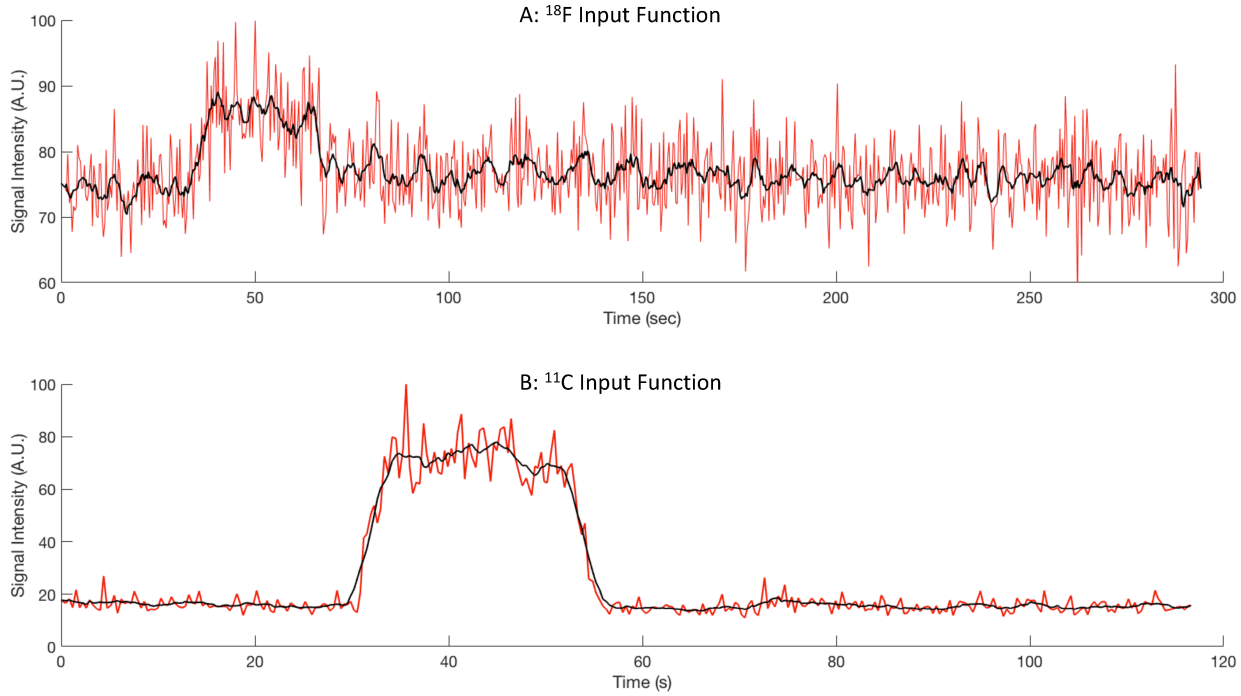

FIGURE 6.3: A: Input function of ^{18}F. B: Input function of ^{11}C. The red lines are the experimental data. The black lines are smoothed curves obtained from a moving average of 5 points.

The red curve on figure 6.4 shows the integrated signal from the oscilloscope over 84 minutes when a solution of ^{11}C is inserted in the phantom. The decay constant extracted from the exponential fit is $(5.63 \pm 0.09)\cdot 10^{-4}$ s^{-1}. The starting point of activity concentration was 3.02 MBq/ml. The uncertainty on the decay constant represents the 95% confidence interval on the fit from Matlab. The black solid curve on figure 6.4 is the fitted decay curve and the black dotted curve is the theoretical decay, normalized to the same value as the fitted curve. The accepted decay constant for ^{11}C is $5.6814\cdot 10^{-4}$

s^{-1}. Both curves coincide almost perfectly.

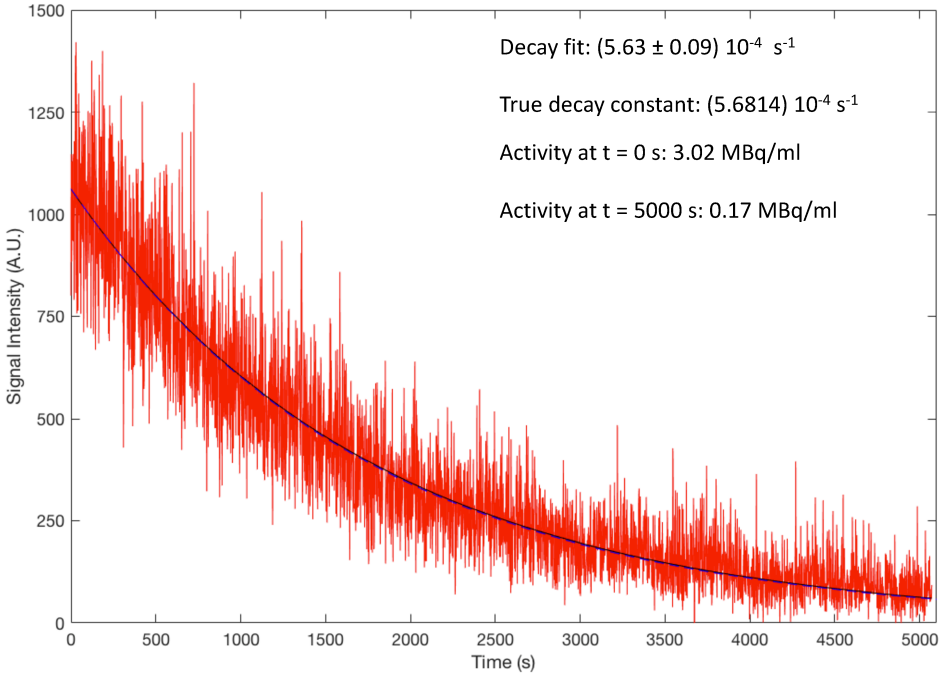

FIGURE 6.4: Decay of ^{11}C measured over 84 minutes with the detector. The red curve represents the experimental data. The black solid and dotted curves are the mono exponential fit and the theoretical decay, respectively. Both curves overlap almost perfectly.

Chapter 7

Discussion

7.1 Detector assembly

The method to manufacture the dual-readout detector was developed at Denmark Technical University and Riso National Laboratory by Dr. Gustavo Kertzscher. It is an inexpensive and simple method that does not require sophisticated and expensive laboratory equipment or intensive training. This will allow an easy implementation of the detector in any institution acquiring dynamic PET images. To protect the intellectual property of the manufacturing methods, the details of the technique are not presented in this thesis.

Plastic scintillating fibers were preferred to inorganic scintillator for two reasons. First, plastic fibers are flexible and can be wrapped around the patient's wrist. Second, scintillating fibers decay constants are on the nanosecond scales (BCF-12 is 3.2 ns), while most commonly used inorganic scintillators decay constants are more than hundreds of nanoseconds (NaI(Tl) is 230 ns) (Knoll, 2000).

For the detector developed in this thesis, BCF-12 scintillating fiber (Saint-Gobain, France) was used as the sensitive part. Its core is made of polystyrene. It was considered as a prime candidate due to its negligible dependency on temperature, memory effect, constant sensitivity and a high spatial resolution (Beddar et al., 2003; Beierholm et

al., 2008). We chose BCF-12 over BCF-60 due to its ability to generate a larger signal and because the blue light produced in the BCF-12 is more attenuated than green light produced in the BCF-60. This is required to maximize the positional resolution for dual read-out detectors. Saint-Gobain has a clear transmission fiber with a core of polystyrene (BCF-98), but the Eska fiber since its core is made of PMMA, which is more robust than polystyrene and known to minimize fluorescent light generation, reducing unwanted background (Boivin et al., 2015). Polystyrene is also known to attenuate visible light more than PMMA.

The light detection device converting the scintillation signal to an electrical signal is a PMT module, model H6779-03. Silicon photomultipliers (SiPM) are gradually replacing PMTs in nuclear medicine applications. Compared to classic PMT, SiPMs offer high gain, high photon efficiency, low operation voltage and can act as digital photon counters due to their excellent timing properties (Gundacker et al., 2012). SiPMs are also approximately 10 times less expensive than PMTs.

The oscilloscope is not the ideal system to record the pulses from a light detection device. On one hand, the fast sampling rate allows accurate modeling of the electrical signal from the PMT without altering the waveform. On the other, it cannot record the complete signal. It took $\approx$ 400 ms to record a 5 ms waveform on the computer. The counting of the individual pulses was investigated using the oscilloscope and the 5 ms waveform. A Matlab function was developed to identify peaks with a minimum height, width and distance from each other. This method yielded similar results as the integration of the waveform, but since it is not possible to acquire the data continuously, the small number of peaks on each waveform resulted on higher uncertainty. Until a continuous acquisition method is implemented, the integration of the waveform will be used.

Gearhart, 2012 used a digital oscilloscope (Tektronix DP07104) to acquire the entire signal, but the price is on the order of \$50 000, making the detector no longer cost-effective. In future versions, the analogue oscilloscope will be replaced by compact and

fast USB digitizer and multichannel analyzers to acquire continuously the signal from the light detection device and perform pulse shaping analysis to distinguish between photons and positron interactions.

7.2 Attenuation measurements

The attenuation length for BCF-12 scintillating fiber is provided by Saint-Gobain in their catalog (Saint-Gobain, 2005). An attenuation length of 270 cm is reported with a ^{90}Sr electron source on a precision track with a servo to control the position to 1 mm. In their catalog, the company specified that the uncertainty on the measurements is within 5%, corresponding to $\pm$ 8 cm for an attenuation length of 270 cm. The single readout measurement in this thesis aims to replicate measurement reported by the company, but with the available ^{137}Cs source. In their catalog, Saint-Gobain specifies that the end of the fiber not connected to the PMT is "darkened to eliminate reflections". In the present case, the reflection could not be eliminated. Therefore, the points beyond 270 cm in figure 6.1 were omitted, as the reflections generated higher signal. The reflections also explain the trend of the last points being higher than the curve plotted using Saint-Gobain attenuation length. The attenuation length obtained with our set-up does correspond to Saint-Gobain, being 278 $\pm$ 49 cm. Because of its large dimension compared to the fiber (25 mm in diameter versus 1 mm for the fiber), it is hard to keep the position of the fiber relative to the source constant without a dedicated precision track, and small a variation in the lateral position of the source can lead to large variation in scintillation light. Using a dual readout setup, these differences are eliminated by normalizing the output at one end by the output at the other.

The attenuation length obtained with the dual readout detectors and a ^{137}Cs source correspond to Saint-Gobain value with 277 $\pm$ 12 cm and 261 $\pm$ 16 cm for the 3.0 m and 1.5 m respectively. However, with the UV light, the attenuation length was overestimated

to 307 $\pm$ 6 cm and 294 $\pm$ 8 cm. Panel C in figure 6.2 clearly shows the divergence between the experimental data and the curves with the attenuation from Saint-Gobain. On panel D, the length of the detector is too short to highlight the difference. Intuitively, the attenuation length should be shorter when using UV light, since the shorter wavelengths are more attenuated, but we observed the opposite. However, the BCF-12 fiber is not pure polystyrene, as it includes the scintillating molecules that absorb the UV light and emit photoluminescence. As a result, the scenario is more complex, with the UV light being attenuated and absorb to generate photoluminescence at longer wavelength. This situation could be further investigated with a different equation for the attenuation, but since the UV spectrum will be absent in clinical situation, it is beyond the scope of this work. UV measurement will uniquely be used for a rapid verification of light transmission in newly built detectors.

The subtraction of the background is also critical to obtain the same attenuation length as Saint-Gobain. Without it, the signal at the furthest ends of the detector is over-estimated and the attenuation length is greatly over-estimated. Without background subtraction, the attenuation length was 434 cm with the ^{137}Cs excitation.

The purpose of using a dual read-out configuration is to determine the position of the positron interaction in the fiber. The amplitude of the signal from each PMT are indicative of the number of photons received and depends on the length of the fiber along which it was transmitted. When taking the ratio of the signal at both ends of the fiber, the position can be determined with the equation:

$$x = \frac{\lambda_a}{2} \cdot \ln\left(\frac{S_2}{S_1}\right) \tag{7.1}$$

In equation 7.1, the position x is defined at 0 at the center of the fiber, with the positive values towards S_2 and the negative values towards S_1. The positions of interaction are used to identify veins and arteries based on the "first pass" of the radiotracer, to

determine the rate at which the radiotracers are traveling along the wrist and to determine the rate of positron emission. Chichester, Watson, and Johnson, 2013 employed scintillating fiber as radiation survey meter over large areas. This group used the timing differences between the arrival of a pulse at each end of a 15 m scintillating fiber to determine the position of the interaction between the radiation and the fiber. The timing resolution was $\approx$ 7 ns, corresponding to a $\approx$ 50 cm spatial resolution for a 1 cm radiation source. In another study, Antonelli, Antonelli, and Barbiellini, 1996 measured a timing resolution of 0.4 ns for a 4 m scintillating fiber, which could result in a spatial resolution as good as 3 cm. Finocchiaro, 2012 developed a scintillating fiber detector to monitor leaks on barrels of radioactive waste. To determine the position of the leakage, the authors envisage crossing scintillating fibers and determining the position of the leak by looking at which fibers gave a signal. In the future studies we will investigate the different methods mentioned above to find the setup with the best spatial resolution.

Previous studies investigated the attenuation length of scintillating fibers. Amos, Bross, and Lundin, 1990 and Hawkes et al., 1990 both investigated the difference in the light transmitted through the cladding and through the core of the fiber. Both studies concluded that the amount of light transmitted through the cladding is higher than inside the core over the first 50 cm of the scintillator. However, the rays traveling the cladding attenuate much faster because of their skewness and it is the core light that dominates at longer distances.

7.3 Bending losses

The smallest uncertainty in measurements obtained with the ^{137}Cs radiation source is 5.4%, but the largest loss is 4.4%. Chung and Margulies, 1995a also obtained losses smaller than their measurements uncertainty when investigating bending losses. Since the light signal from the UV lamp is much higher and constant than the scintillation

signal from the used weak ^{137}Cs source (186.5 kBq), it is possible to see the relation between the bending radius and the light loss. A previous study by Chung and Margulies, 1995b reported bending losses in Kuraray scintillating fibers on the order 1% for bending radius of 6 cm and larger losses as the bending radius decreased down to 1 cm. In the present work, smaller radius are not useful as a human hand needs to be slipped inside the loops for the detector to be used on patients. Chung and Margulies, 1995a also concluded that the attenuation length did not change over 3.5 years for Kuraray fibers properly stored and the bending losses did not change for fibers kept bent in coils with 10 turns and a radius of 3 cm for a year. Finally, when (Chung and Margulies, 1995b) investigated the losses for multiple loops in a 0.965 mm diameter Kuraray fiber, additional losses smaller than 2% for 10 loops with a radius of 3.5 cm were observed. Therefore, it is fair to conclude that even with five loops in the scintillating fiber, the losses due to the changes in the shape of the fiber will be negligible.

7.4 Phantom measurements

The increase in signal as the solution arrive in the phantom can be seen with both radioactive solution. The slopes on the side of the step function comes from the finite time required to detect the entire solution. The better SNR when measuring ^{11}C can be explained with the longer range of its positrons. The maximum range of positrons from ^{11}C is 4.456 mm, in contrast to 2.633 mm for the ^{18}F. The increase in SNR confirms that it is easier to detect isotopes emitting positrons of higher energy, and therefore longer range. Other commonly used radionuclides in PET such as ^{13}N, ^{15}O and ^{68}Ga, have even longer maximum range for their positrons, 5.752 mm, 9.132 mm and 10.273 mm respectively. Future work will include repeating the phantom measurements with these radionuclides to further investigate the detector sensitivity.

Shokouhi et al., 2003 made a similar measurement with LSO crystals to image the signal in a wrist phantom. The edges of their square input functions were less sharp than

the one presented with the detector developed in this thesis. The authors do not specify the time it takes their detector to generate images, but they state: "Here the activity was allowed to decay in place in the tubing to simulate an image with a long acquisition time". Because PET images are acquired with a long enough time to increase the SNR, it is fair to assume that their time resolution is slower than 2.87 points per second. When the electronics for the detector developed in this thesis will be optimized to have continuous readings, the timing resolution will be even better, which is crucial to have a precise definition of the AIF peak.

In the future, a wrist phantom with a pump will be developed to simulate the circulation of blood and the dispersion of the AIF as it travels through the blood vessels.

The measured decay constant of $(5.63 \pm 0.09) \cdot 10^{-4}$ s^{-1} corresponds to the accepted value of $5.6814 \cdot 10^{-4}$ s^{-1}. If the background levels are not subtracted, it results in an under-estimation of the decay constant. The decay constant without background subtraction is $(3.00 \pm 0.05) \cdot 10^{-4}$ s^{-1}. The response of the detector needs to be evaluated for activity concentrations even lower than what was used in this study, as the final activity concentration for figure 6.4 is 0.17 MBq/ml, and the blood activity concentration in PET studies is around 0.09 MBq/ml according to Villanueva et al., 2003. With a continuous reading, the sensitivity might be increased enough to allow for a better representation of lower radioactivity concentrations. Other alternatives to increase the sensitivity are to use light detection devices with higher gain or efficiency or even to use amplifiers after the light detection device.

7.5 Plasma and whole-blood activity

The detector only offers a measure of the relative concentration of activity. As stated by Pain et al., 2004 and Lee et al., 2008, the sensitivity of a radiation detector will depend on the size and the depth of the radial and ulnar arteries. Therefore, the relationship between the detector signal and absolute radioactivity concentration will be different

for each patient. Most studies on non-invasive determination of the AIF use a late blood sample to normalize their AIF (Watabe et al., 1995; Yamamoto et al., 1999; Pain et al., 2004; Kriplani et al., 2006). With their detector, Kriplani et al., 2006 measured the detector's efficiency to be 0.108 count per second (cps) per Bq/ml injected (4 cps per nCi/cc, as specified in the article), resulting in a measured peak activity concentration of 10.36 kBq/ml (280 nCi/cc). However, with manual sampling, the paper states a peak activity concentration of 40.7 kBq/ml (1100 nCi/cc), proving the need for normalization. Just as with the PET data, the AIF will need to be corrected for the radioactive decay of the tracer. Additional corrections for delay between the response in the radial and ulnar arteries and the response in the studied tissue, such as the brain in cerebral blood flow study, might be needed. This correction is also needed when performing manual blood sampling. A correction method using an inverse Laplace transform was proposed by Iida et al., 1986.

When recording the AIF in the arteries, it is the concentration of activity in the whole blood volume that is measured. This is fine for radiotracers like $H_2{}^{15}O$ which freely diffuse in the entire volume, but as mention earlier, the pharmacokinetics of FDG requires the plasma activity concentration. For manual blood sampling, the samples are centrifuged to separate the plasma from the other components and its activity directly measured. For automatic blood sampling, the standard is to multiply the input function with the ratio of plasma to whole blood radioactivity. This ratio is obtained through manual blood sample for several subjects and a population based correction curve is derived (Pain et al., 2004; Dhawan et al., 1994; Weber et al., 2002). However, these studies were performed on rodents where, according to Ashworth et al., 1996, the plasma to whole blood ratio changes over time, in contrast to humans. Therefore, the late blood sample needed for quantifying the absolute radioactivity concentration can also serve to determine the plasma to whole blood ratio when the study requires it.

7.6 Cerenkov radiation

When working with optical fibers and ionizing radiation, an additional background contribution can be observed. When a charged particle travels faster than the speed of light in a medium, it emits light known as Cerenkov radiation (Jelley, 1955). With BCF-12, the threshold energy for electrons and positrons to generate Cerenkov radiation is 144 keV (Pain et al., 2002). The positrons and secondary electrons generated by the 511 keV photons will be able to generate Cerenkov radiation, adding an unwanted background to the scintillation signal. Many studies with optical fibers in the fields of dosimetry and radiation detection have investigated the contribution of Cerenkov radiation. Goulet, Gingras, and Beaulieu, 2011 used a plastic scintillator array to monitor the opening of a linac's multileaf collimator. The Cerenkov contribution was considered negligible since no clear optical fiber was directly in the radiation beam's path and the amount of Cerenkov light produced per unit length of irradiated plastic is very small compared to the scintillation light signal. In their study of a β^+ microprobe, Pain et al., 2000 measured that 90% of the Cerenkov radiation only yields 1 photoelectron, while the mean value for scintillating signal was 4 photoelectrons. Setting a threshold above 1 photoelectron allowed them to reduce the Cerenkov component to 0.01% per millimeter of optical fiber irradiated. In their following study (Pain et al., 2002), the authors measured the effect of Cerenkov radiation by immersing a piece of clear optical fiber in a uniform ^{18}F solution.

The maximum intensity of Cerenkov radiation is in the UV range. By using an optical filter with a cut-off at 400 nm, the Cerenkov signal fell to 65%, while the scintillating signal was kept at 90%. The Cerenkov light from a 4 mm clear fiber was only 7% of the signal from a 1 mm scintillating tip. With these results and the actual distribution of radiation interacting with the clear fiber presenting far less background than immersing the fiber in a ^{18}F solution, Pain et al., 2002 conclude that the Cerenkov signal will not contribute significantly.

One method to evaluate the amount of Cerenkov radiation is to build a detector with a polystyrene transmission fiber (BCF-98, Saint-Gobain) instead of the scintillating fiber. Without scintillating molecules, the only light reaching the PMTs will come from Cerenkov radiation.

Chapter 8

Conclusion

This thesis covered the interactions of two types of ionizing radiation: photons and light charged particles. Different gas filled detectors based on the leaky capacitor, semiconductor detectors working as solid-state gas filled detectors and finally scintillation detectors were presented. Principles of PET as well as the difference between static and dynamic acquisitions were discussed. The basics of pharmacokinetic modeling based on compartmental models were introduced. The main limitation of pharmacokinetic modeling comes from the need to determine the AIF. The problems associated with the determination of the AIF and the current alternatives were described in chapter four.

The objective of this thesis was to present the work done on a non-invasive positron detector based on plastic scintillating fibers in a dual readout configuration to monitor the AIF in PET. The attenuation of the light signal in the scintillating fiber can be accurately measured with the present detector set-up and a ^{137}Cs gamma source. With improved electronics to record the visible light signal from the scintillation, it may be possible to monitor individual events and find their point of emission in the scintillating fiber based on the ratio of the signal at each end of the detector. In accordance with previous studies, bending the scintillating fiber will only cause negligible signal losses and the scintillating fiber will not be under enough stress to cause important damage. The response of the detector to two PET radionuclides (^{18}F and ^{11}C) was tested with a simple, first pass, input function. The longer range of the positrons emitted from

^{11}C allows for a less noisy input function to be recorded. The detector was also able to accurately measure the decay constant of ^{11}C to (5.63 $\pm$ 0.09) $\cdot 10^{-4}$ s^{-1}, which coincide with the accepted value of 5.6814 $\cdot 10^{-4}$ s^{-1}. This measurement covered activity concentrations from 3.02 MBq/ml to 0.17 MBq/ml.

The results obtained by the first prototype of the detector are encouraging and demonstrate that the acquisition of the AIF in dynamic PET imaging can potentially be done with a non-invasive detector based on scintillating fibers. Future work will include improvement of the electronics to go from an integrated signal to counting the individual pulses of visible light coming from the scintillation process. To distinguish between positron and gamma ray interactions in the scintillating fiber, pulse shape and pulse height analysis will be enabled. Other visible light detection device than PMTs, such as SiPMs, and development of a realistic wrist phantom constructed of a water equivalent material with arteries and veins, as well as a pumping system to recreate a circulating blood motion will be investigated. Phantom measurements with additional PET radionuclide based on ^{13}N and ^{15}O will be performed. Finally, the detector will be assembled in a sleeve-like cylinder to be tested on patients, as its non-invasiveness makes it easy to integrate in clinical trials. The AIF obtained with blood sampling will be compared to the one provided by the proposed detector.

Bibliography

Afshar-Oromieh, A. et al. (2013). “PET imaging with a [68Ga]gallium-labelled PSMA ligand for the diagnosis of prostate cancer: biodistribution in humans and first evaluation of tumour lesions.” In: *European journal of nuclear medicine and molecular imaging* 40.4, pp. 486–495. ISSN: 16197089. DOI: 10.1007/s00259-012-2298-2. URL: http://link.springer.com/10.1007/s00259-012-2298-2.

Amos, N A, A D Bross, and M C Lundin (1990). “Optical attenuation length measurements of scintillating fibers”. In: *Nuclear Inst. and Methods in Physics Research, A* 297.3, pp. 396–403. ISSN: 01689002. DOI: 10.1016/0168-9002(90)91321-2.

Antonelli, A., M. Antonelli, and G. Barbiellini (1996). “Measurements of light yield, attenuation length and time response of long samples of "blue" scintillating fibers”. In: *Nuclear Instruments and Methods in Physics Research, Section A: Accelerators, Spectrometers, Detectors and Associated Equipment* 370.2-3, pp. 367–371. ISSN: 01689002. DOI: 10.1016/0168-9002(95)00806-3.

Archambault, Louis et al. (2005). “Plastic scintillation dosimetry: optimal selection of scintillating fibers and scintillators”. In: *Medical Physics* 32.7, pp. 2271–2278. ISSN: 00942405. DOI: 10.1118/1.1943807.

Ashworth, Sharon et al. (1996). “Development of an On-Line Blood Detector System for PET Studies in Small Animals”. In: *Technology*, pp. 62–66. DOI: 10.1016/B978-012389760-2/50015-3. URL: http://www.sciencedirect.com.proxy3.library.mcgill.ca/science/article/pii/B9780123897602500153.

Attix, Frank Herbert (2007). “Quantities for Describing the Interaction of Ionizing Radiation with Matter”. In: *Introduction to Radiological Physics and Radiation Dosimetry*. Weinheim, Germany: Wiley-VCH Verlag GmbH, pp. 20–37. ISBN: 9783527617135.

DOI: 10.1002/9783527617135.ch2. URL: http://doi.wiley.com/10.1002/9783527617135.ch2http://dx.doi.org/10.1002/9783527617135.ch2.

Beddar, Sam et al. (2003). "Plastic scintillation dosimetry: optimization of light collection efficiency." In: *Physics in medicine and biology* 48.9, pp. 1141–52. ISSN: 0031-9155. DOI: 10.1088/0031-9155/48/9/305. URL: http://www.ncbi.nlm.nih.gov/pubmed/12765328.

Beierholm, Anders R. et al. (2008). "A comparison of BCF-12 organic scintillators and Al2O3:C crystals for real-time medical dosimetry". In: *Radiation Measurements* 43.2-6, pp. 898–903. ISSN: 13504487. DOI: 10.1016/j.radmeas.2007.12.032. URL: http://linkinghub.elsevier.com/retrieve/pii/S135044870700563X.

Bentourkia, M'hamed (2010). "Tracer Kinetic Modeling: Methodology and Applications". In: *Basic Sciences of Nuclear Medicine*. Berlin, Heidelberg: Springer Berlin Heidelberg, pp. 353–376. DOI: 10.1007/978-3-540-85962-8{_}17. URL: http://link.springer.com/10.1007/978-3-540-85962-8_17.

Berger, M J and S M Seltzer (1983). "Stopping powers and ranges of electrons and positrons". In: *Vol NBSIR 82-2550*. URL: http://adsabs.harvard.edu/abs/1982spre.reptQ....B%5Cnpapers3://publication/uuid/AA3C254A-3616-4C3B-B499-62C1DB96598B.

Boellaard, R. et al. (2001). "Characteristics of a new fully programmable blood sampling device for monitoring blood radioactivity during PET". In: *European Journal of Nuclear Medicine* 28.1, pp. 81–89. ISSN: 03406997. DOI: 10.1007/s002590000405.

Boivin, Jonathan et al. (2015). "Systematic evaluation of photodetector performance for plastic scintillation dosimetry". In: *Medical Physics* 42.11, pp. 6211–6220. ISSN: 00942405. DOI: 10.1118/1.4931979. URL: http://doi.wiley.com/10.1118/1.4931979.

Carson, R E (1991). "The development and application of mathematical models in nuclear medicine." In: *Journal of nuclear medicine : official publication, Society of Nuclear*

Medicine 32.12, pp. 2206–8. ISSN: 0161-5505. URL: http://www.ncbi.nlm.nih.gov/pubmed/1744704.

Champion, C and C Le Loirec (2007). "Positron follow-up in liquid water: II. Spatial and energetic study for the most important radioisotopes used in PET". In: *Physics in Medicine and Biology* 52.22, pp. 6605–6625. ISSN: 00319155. DOI: 10.1088/0031-9155/52/22/004. URL: http://stacks.iop.org/0031-9155/52/i=22/a=004?key=crossref.1daf17f2e1836466fb122a3a39da746d.

Cherry, Simon R., James A. Sorenson, and Phelps (2012). "Interaction Radiation Matter". In: *Physics in Nuclear Medicine*. Elsevier, pp. 63–85. ISBN: 9781416051985. DOI: 10.1016/B978-1-4160-5198-5.00006-X. URL: http://linkinghub.elsevier.com/retrieve/pii/B978141605198500006X.

Cherry, Simon R., James A. Sorenson, and Michael E. Phelps (2012a). "Positron Emission Tomography". In: *Physics in Nuclear Medicine*, pp. 307–343. ISBN: 978-1-4160-5198-5. DOI: 10.1016/B978-1-4160-5198-5.00018-6. URL: https://ac-els-cdn-com.proxy3.library.mcgill.ca/B9781416051985000186/3-s2.0-B9781416051985000186-main.pdf?_tid=a63c57b6-29fc-4f98-8e47-58fb7673076a&acdnat=1520194677_4fe0f321b39c17c7806156468e433dcchttp://linkinghub.elsevier.com/retrieve/pii/B97814160519.

– (2012b). "Radiation Detectors". In: *Physics in Nuclear Medicine*, pp. 87–106. ISBN: 9781416051985. DOI: 10.1016/B978-1-4160-5198-5.00007-1. URL: https://ac-els-cdn-com.proxy3.library.mcgill.ca/B9781416051985000071/3-s2.0-B9781416051985000071-main.pdf?_tid=de33f6c6-0eed-4675-969c-a043130602e1&acdnat=1520607144_cdc158e8ea5c636ec65ad7fbb61d941bhttp://linkinghub.elsevier.com/retrieve/pii/B97814160519.

– (2012c). "Tracer Kinetic Modeling". In: *Physics in Nuclear Medicine*, pp. 379–405. ISBN: 978-1-4160-5198-5. DOI: 10.1016/B978-1-4160-5198-5.00021-6. URL: http://www.sciencedirect.com.proxy3.library.mcgill.ca/science/article/pii/B9781416051985000216http://linkinghub.elsevier.com/retrieve/pii/B9781416051985000216.

Chichester, David L., Scott M. Watson, and James T. Johnson (2013). "Comparison of bcf-10, bcf-12, and bcf-20 scintillating fibers for use in a 1-dimensional linear sensor". In: *IEEE Transactions on Nuclear Science* 60.5, pp. 4015–4021. ISSN: 00189499. DOI: 10.1109/TNS.2013.2277799.

Chung, M and S Margulies (1995a). "Aging studies on stressed and unstressed scintillating, wave-shifting, and clear fibers". In: 2551, pp. 2–9.

– (1995b). "Effects of Stress and Strain on Scintillating and Clear Fibers". In: *IEEE Transactions on Nuclear Science* 42.4, pp. 323–327.

Derlon, Jean-Michel et al. (1989). "[11C]l-Methionine Uptake in Gliomas". In: *Neurosurgery* 25.5, pp. 720–728. ISSN: 0148-396X. DOI: 10.1227/00006123-198911000-00006. URL: https://academic.oup.com/neurosurgery/article-lookup/doi/10.1227/00006123-198911000-00006.

Dhawan, V et al. (1994). "Quantitative brain FDG/PET studies using dynamic aortic imaging". In: *Physics in medicine and biology* 39.9, pp. 1475–1487. ISSN: 0031-9155. DOI: 10.1088/0031-9155/39/9/012. URL: http://iopscience.iop.org.proxy3.library.mcgill.ca/article/10.1088/0031-9155/39/9/012/pdfhttp://www.iop.org/EJ/abstract/0031-9155/39/9/012/%5Cnpapers://39e074f5-8b59-44fd-a30c-0ca49bed9220/Paper/p1309.

Erlandsson, Kjell (2010). "Tracer Kinetic Modeling: Basics and Concepts". In: *Basic Sciences of Nuclear Medicine*. Berlin, Heidelberg: Springer Berlin Heidelberg, pp. 333–351. DOI: 10.1007/978-3-540-85962-8{_}16. URL: http://link.springer.com/10.1007/978-3-540-85962-8_16.

Feng, D et al. (1997). "A technique for extracting physiological parameters and the required input function simultaneously from PET image measurements: theory and simulation study." In: *IEEE transactions on information technology in biomedicine : a publication of the IEEE Engineering in Medicine and Biology Society* 1.4, pp. 243–254. ISSN: 1089-7771. DOI: 10.1109/4233.681168.

Finocchiaro, Paolo (2012). *DMNR: A new concept for real-time online monitoring of short and medium term radioactive waste*, pp. 1–40. ISBN: 9781621001881. URL: http://www.innovatoripa.it/sites/default/files/capitolo_libro.pdf.

Gearhart, Joel S. (2012). "Investigation of BCF-12 plastic scintillating coherent fiber bundle timing properties". PhD thesis. URL: http://www.dtic.mil/dtic/tr/fulltext/u2/a558322.pdf.

Goulet, Mathieu, Luc Gingras, and Luc Beaulieu (2011). "Real-time verification of multileaf collimator-driven radiotherapy using a novel optical attenuation-based fluence monitor". In: *Medical Physics* 38.3, p. 1459. ISSN: 00942405. DOI: 10.1118/1.3549766.

Greuter, Henri N J M et al. (2003). "Measurement of 18F-FDG concentrations in blood samples: comparison of direct calibration and standard solution methods." In: *Journal of nuclear medicine technology* 31.4, pp. 206–9. ISSN: 0091-4916. URL: http://www.ncbi.nlm.nih.gov/pubmed/14657286.

Gundacker, S et al. (2012). "SiPM Photodetectors for Highest Time Resolution in PET SiPM in TOF-PET". In: *PoS*. URL: http://pos.sissa.it/.

Hawkes, C. M. et al. (1990). "Decay time and light yield measurements for plastic scintillating fibers". In: *Nuclear Inst. and Methods in Physics Research, A* 292.2, pp. 329–336. ISSN: 01689002. DOI: 10.1016/0168-9002(90)90388-M.

Hnatowich, D J (1977). "A review of radiopharmaceutical development with short-lived generator-produced radionuclides other than 99mTc". In: *The International Journal Of Applied Radiation And Isotopes* 28.1-2, pp. 169–181. ISSN: 0020708X. DOI: 10.1016/0020-708X(77)90171-5. URL: http://ac.els-cdn.com.proxy3.library.mcgill.ca/0020708X77901715/1-s2.0-0020708X77901715-main.pdf?_tid=e314099e-76d3-11e7-921e-00000aacb362&acdnat=1501603988_2592d4ffa14825baf7050c8e39ab5fe5.

Hubbell, J.H. and S.M. Seltzer (1996). *NIST: X-Ray Mass Attenuation Coefficients*. URL: http://www.nist.gov/pml/data/xraycoef/.

Iida, Hidehiro et al. (1986). "Error analysis of a quantitative cerebral blood flow measurement using H2(15)O autoradiography and positron emission tomography, with respect to the dispersion of the input function." In: *Journal of cerebral blood flow and metabolism : official journal of the International Society of Cerebral Blood Flow and Metabolism* 6.5, pp. 536–545. ISSN: 0271-678X. DOI: 10.1038/jcbfm.1986.99. URL: http://journals.sagepub.com/doi/pdf/10.1038/jcbfm.1986.99.

Jelley, J V (1955). "Cerenkov radiation and its applications". In: *British Journal of Applied Physics* 6.7, p. 227. ISSN: 0508-3443. DOI: 10.1088/0508-3443/6/7/301. URL: http://stacks.iop.org/0508-3443/6/i=7/a=301.

Jons, Peter H. et al. (1997). "Follow-up of radial arterial catheterization for positron emission tomography studies". In: *Human Brain Mapping* 5.2, pp. 119–123. ISSN: 10659471. DOI: 10.1002/(SICI)1097-0193(1997)5:2<119::AID-HBM5>3.0.CO;2-6.

Khalil, Magdy M. (2010a). "Emission Tomography and Image Reconstruction". In: *Basic Sciences of Nuclear Medicine*. Berlin, Heidelberg: Springer Berlin Heidelberg, pp. 259–284. DOI: 10.1007/978-3-540-85962-8{_}13. URL: http://link.springer.com/10.1007/978-3-540-85962-8_13.

– (2010b). "Positron Emission Tomography (PET): Basic Principles". In: *Basic Sciences of Nuclear Medicine*. Berlin, Heidelberg: Springer Berlin Heidelberg, pp. 179–213. DOI: 10.1007/978-3-540-85962-8{_}11. URL: http://link.springer.com/10.1007/978-3-540-85962-8_11.

Khan, N et al. (2011). "18F-fluorodeoxyglucose uptake in tumor." In: *Mymensingh medical journal : MMJ* 20.2, pp. 332–42. ISSN: 1022-4742. URL: http://www.ncbi.nlm.nih.gov/pubmed/21522112.

Knoll, Glenn F (2000). *Radiation Detection and Measurement*. Vol. 3, p. 860. ISBN: 9780470131480. DOI: 10.1017/CBO9781107415324.004. URL: http://www.wiley.com/WileyCDA/WileyTitle/productCd-EHEP001606,descCd-OVERVIEW.html.

Kriplani, A. et al. (2006). "Non-invasive and selective measurement of the arterial input function using a PET Wrist Scanner". In: *2006 IEEE Nuclear Science Symposium Conference Record*, pp. 3266–3270. DOI: 10.1109/NSSMIC.2006.353705. URL: http:

//ieeexplore.ieee.org/lpdocs/epic03/wrapper.htm?arnumber=4179747.

Kurudirek, Murat (2014). "Effective atomic numbers and electron densities of some human tissues and dosimetric materials for mean energies of various radiation sources relevant to radiotherapy and medical applications". In: *Radiation Physics and Chemistry* 102, pp. 139–146. ISSN: 0969-806X. DOI: 10.1016/J.RADPHYSCHEM.2014.04.033. URL: https://www.sciencedirect.com/science/article/pii/S0969806X14001613?_rdoc=1&_fmt=high&_origin=gateway&_docanchor=&md5=b8429449ccfc9c30159a5f9aeaa92ffb#t0010.

Lecoq, Paul, Mikhael Korzhik, and Andrey Vasiliev (2014). "Can transient phenomena help improving time resolution in scintillators?" In: *IEEE Transactions on Nuclear Science* 61.1, pp. 229–234. ISSN: 00189499. DOI: 10.1109/TNS.2013.2282232.

Lee, Dongchul et al. (2016). "Ultrasound evaluation of the radial artery for arterial catheterization in healthy anesthetized patients". In: *Journal of Clinical Monitoring and Computing* 30.2, pp. 215–219. ISSN: 1387-1307. DOI: 10.1007/s10877-015-9704-9. URL: http://link.springer.com/10.1007/s10877-015-9704-9.

Lee, Kihak et al. (2008). "A positron-probe system for arterial input function quantification for positron emission tomography in humans". In: *Review of Scientific Instruments* 79.6. ISSN: 00346748. DOI: 10.1063/1.2936880.

Levin, Craig S and Edward J Hoffman (1999). "Calculation of positron range and its effect on the fundamental limit of positron emission tomography system spatial resolution Calculation of positron range and its effect on the fundamental limit of positron emission tomography system spatial resolution". In: *Phys. Med. Biol.* 44.99, pp. 781–799. URL: https://pdfs.semanticscholar.org/1ac7/b6e56311d23a2902fd63c pdf.

Lin, K P et al. (1995). "Correction of spillover radioactivities for estimation of the blood time-activity curve from the imaged LV chamber in cardiac dynamic FDG PET studies." In: *Physics in medicine and biology* 40.4, pp. 629–42. ISSN: 0031-9155. URL: http://www.ncbi.nlm.nih.gov/pubmed/7610118.

Litton, J E and L Eriksson (1990). "Transcutaneous measurement of the arterial input function in positron emission tomography". In: *IEEE Trans Nucl Sci* 37.2, pp. 627–628.

Mintun, M a et al. (1984). "Brain oxygen utilization measured with O-15 radiotracers and positron emission tomography." In: *Journal of nuclear medicine : official publication, Society of Nuclear Medicine* 25.2, pp. 177–187. ISSN: 0161-5505. DOI: 10.1016/j.cortex.2011.07.006.

Muzi, Mark et al. (2012). "Quantitative assessment of dynamic PET imaging data in cancer imaging". In: *Magnetic Resonance Imaging* 30.9, pp. 1203–1215. ISSN: 0730725X. DOI: 10.1016/j.mri.2012.05.008. URL: http://linkinghub.elsevier.com/retrieve/pii/S0730725X12001944.

Online, Oxford English Dictionary (2010). *Oxford English Dictionary Online*. Vol. 2010. 07/07, http://dictionary.oed.com/. ISBN: 15424715. URL: http://dictionary.oed.com.

Pain, F. et al. (2000). "SIC, an intracerebral radiosensitive probe for in vivo neuropharmacology investigations in small laboratory animals: theoretical considerations and practical characteristics". In: *IEEE Transactions on Nuclear Science* 47.1, pp. 25–32. ISSN: 00189499. DOI: 10.1109/23.826894. URL: http://ieeexplore.ieee.org/document/826894/.

Pain, F. et al. (2002). "SIC: An intracerebral radiosensitive probe for in vivo neuropharmacology investigations in small laboratory animals: Prototype design, characterization, and in vivo evaluation". In: *IEEE Transactions on Nuclear Science* 49 I.3, pp. 822–826. ISSN: 00189499. DOI: 10.1109/TNS.2002.1039570.

Pain, Frédéric et al. (2004). "Arterial input function measurement without blood sampling using a beta-microprobe in rats." In: *Journal of nuclear medicine : official publication, Society of Nuclear Medicine* 45.9, pp. 1577–82. ISSN: 0161-5505. DOI: 45/9/1577[pii]. URL: http://www.ncbi.nlm.nih.gov/pubmed/15347727.

Phelps, M. E. et al. (1979). "Tomographic measurement of local cerebral glucose metabolic rate in humans with (F-18)2-fluoro-2-deoxy-D-glucose: Validation of method". In: *Annals of Neurology* 6.5, pp. 371–388. ISSN: 15318249. DOI: 10.1002/ana.410060502.

URL: http://www.ncbi.nlm.nih.gov/pubmed/117743http://doi.wiley.com/10.1002/ana.410060502.

Podgorsak, Ervin B. (2006). "Radiation Physics for Medical Physicists". In: *Medical Physics* 33.1, p. 249. ISSN: 00942405. DOI: 10.1118/1.2142596.

Rontgen and W. C. (1896). "ON A NEW KIND OF RAYS". In: *Science* 3.59, pp. 227–231. ISSN: 0036-8075. DOI: 10.1126/science.3.59.227. URL: http://www.sciencemag.org/cgi/doi/10.1126/science.3.59.227.

Saint-Gobain (2005). "Scintillating Optical Fibers". In: pp. 1–6.

Schelbert, H R et al. (1981). "N-13 ammonia as an indicator of myocardial blood flow." In: *Circulation* 63.6. URL: http://circ.ahajournals.org.proxy3.library.mcgill.ca/content/63/6/1259.

Shokouhi, S. et al. (2003). "A Noninvasive LSO-APD Blood Radioactivity Monitor for PET Imaging Studies". In: *IEEE Transactions on Nuclear Science* 50.5, pp. 1457–1461. ISSN: 0018-9499. DOI: 10.1109/TNS.2003.817284. URL: http://ieeexplore.ieee.org/document/1236949/.

T. Bushberg, Jerrold et al. (2011). *The Essential Physics of Medical Imaging*, p. 1030. ISBN: 978-0781780575. URL: https://books.google.ca/books?hl=fr&lr=&id=tqM8IG3f8bsC&oi=fnd&pg=PR1&dq=bushberg&ots=9njy4YjTnm&sig=-8aBt0FkFaLouBpKWDa7xYMGqQg#v=onepage&q=bushberg&f=false.

Takikawa, Shugo et al. (1993). "Noninvasive quantitative fluorodeoxyglucose PET studies with an estimated input function derived from a population-based arterial blood curve." In: *Radiology* 188.1, pp. 131–136. ISSN: 0033-8419. DOI: 10.1148/radiology.188.1.8511286. URL: https://www.researchgate.net/profile/Vijay_Dhawan3/publication/14688605_Takikawa_S_Dhawan_V_Spetsieris_P_Robeson_W_Chaly_T_Dahl_R_Margouleff_D_Eidelberg_DNoninvasive_quantitative_fluorodeoxyglucose_PET_studies_with_an_estimated_input_function_derived_from.

Taylor, John R. (1997). "An Introduction to Error Analysis". In: *Journal of the Acoustical Society of America* 101, p. 330. ISSN: 00014966. DOI: 10.1121/1.418074. URL: http://link.aip.org/link/?JAS/101/1779/1&Agg=doi.

Thie, Joseph A (2004). "Understanding the standardized uptake value, its methods, and implications for usage." In: *Journal of nuclear medicine : official publication, Society of Nuclear Medicine* 45.9, pp. 1431–4. ISSN: 0161-5505. URL: http://www.ncbi.nlm.nih.gov/pubmed/15347707.

Villanueva, A. et al. (2003). "Spatial resolution of a noninvasive measurement of the arterial and venous input function using a wrist monitor". In: *2003 IEEE Nuclear Science Symposium. Conference Record (IEEE Cat. No.03CH37515)*. IEEE, pp. 2232–2236. ISBN: 0-7803-8257-9. DOI: 10.1109/NSSMIC.2003.1352343. URL: http://ieeexplore.ieee.org/document/1352343/papers2://publication/uuid/B017D670-72E1-45FF-AFF5-DB0D302C5A03%5Cnhttp://ieeexplore.ieee.org/lpdocs/epic03/wrapper.htm?arnumber=1352343.

Watabe, H. et al. (1995). "Development of skin surface radiation detector system to monitor radioactivity in arterial blood along with positron emission tomography". In: *IEEE Transactions on Nuclear Science* 42.4, pp. 1455–1459. ISSN: 00189499. DOI: 10.1109/23.467729. URL: http://ieeexplore.ieee.org/lpdocs/epic03/wrapper.htm?arnumber=467729.

Weber, Bruno et al. (2002). "A femoral arteriovenous shunt facilitates arterial whole blood sampling in animals". In: *European Journal of Nuclear Medicine* 29.3, pp. 319–323. ISSN: 03406997. DOI: 10.1007/s00259-001-0712-2. URL: https://link-springer-com.proxy3.library.mcgill.ca/content/pdf/10.1007%2Fs00259-001-0712-2.pdf.

Weber, Wolfgang A. et al. (2000). "O-(2-[18F]fluoroethyl)-L-tyrosine and L-[methyl-11C]methionine uptake in brain tumours: initial results of a comparative study." In: *European journal of nuclear medicine* 27.5, pp. 542–9. ISSN: 0340-6997. DOI: 10.1007/s002590050541. URL: http://link.springer.com/10.1007/s002590050541http://www.ncbi.nlm.nih.gov/pubmed/10853810.

Yamamoto, S. et al. (1999). "Imaging of an artery from skin surface using beta camera". In: *IEEE Transactions on Nuclear Science* 46.3 PART 2, pp. 583–586. ISSN: 00189499. DOI: 10.1109/23.775583.

Yamamoto, Seiichi et al. (2005). "Preliminary study for the development of a tweezers-type coincidence detector for tumor detection". In: *Nuclear Instruments and Methods in Physics Research, Section A: Accelerators, Spectrometers, Detectors and Associated Equipment* 548.3, pp. 564–570. ISSN: 01689002. DOI: 10.1016/j.nima.2005.04.068.

Zanotti-Fregonara, Paolo et al. (2009). "Comparison of eight methods for the estimation of the image-derived input function in dynamic [18F]-FDG PET human brain studies". In: *Journal of Cerebral Blood Flow and Metabolism* 29.11, pp. 1825–1835. ISSN: 0271678X. DOI: 10.1038/jcbfm.2009.93. URL: http://journals.sagepub.com/doi/pdf/10.1038/jcbfm.2009.93.